Flotation and free surface flow in a model for subglacial drainage. Part I: Distributed drainage

By Christian Schoof, Ian J. Hewitt and Mauro A. Werder

Department of Earth and Ocean Sciences, University of British Columbia, 6339 Stores Road,
Vancouver, BC, V6T 1Z4, Canada
Department of Mathematics, University of British Columbia, 1984 Mathematics Road,
Vancouver, BC, V6T 1Z2, Canada
Department of Earth Sciences, Simon Fraser University, 8888 University Drive, Burnaby, BC,
V5A 1S6, Canada

We present a continuum model for melt water drainage through a spatially distributed system of connected subglacial cavities, and consider in this context the complications introduced when effective pressure or water pressure drops to zero. Instead of unphysically allowing water pressure to become negative, we model the formation of a partially vapour- or air-filled space between ice and bed. Likewise, instead of allowing sustained negative effective pressures, we allow ice to separate from the bed at zero effective pressure. The resulting model is a free boundary problem in which an elliptic obstacle problem determines hydraulic potential, and therefore also determines regions of zero effective pressure and zero water pressure. This is coupled with a transport problem for stored water, and the coupled system bears some similarities with Hele-Shaw and squeeze film models. We present a numerical method for computing time-dependent solutions, and find close agreement with semi-analytical travelling wave and steady state solutions. As may be expected, we find that ice-bed separation is favoured by high fluxes and low ice surface slopes and low bed slopes, while partially filled cavities are favoured by low fluxes and high slopes. At the boundaries of regions with zero water or effective pressure, discontinuities in water level are frequently present, either in the form of propagating shocks or as stationary hydraulic jumps accompanied by discontinuities in potential gradient.

1. Introduction

Sliding at the interface between ice and glacier bed is often a significant component in the flow of land-based ice masses. Many fast ice flow phenomena are linked to sliding: the motion of ice streams (bands of fast-moving ice within large ice sheets that drain a larger area of surrounding, more slowly flowing ice, see Alley & Bindschadler (2001)) is often caused almost entirely by slip at the bed (Engelhardt & Kamb 1997). Similarly, glacier surges involve temporal rather than spatial variations in sliding motion, with a single glacier undergoing a relaxation oscillation as it switches from a slow sliding to a fast sliding mode and back again (Kamb *et al.* 1985; Fowler 1987, 1989).

Significant sliding typically occurs when the base of the ice reaches the melting point. Spatial as well as temporal variability in glacier sliding can therefore be caused by temperature changes at the bed (Clarke 1976; MacAyeal 1993; Cuffey *et al.* 1999; Fowler *et al.* 2001). However, there is strong field evidence that sliding is not controlled purely

by the presence or absence of liquid water at the ice-bed interface, but that subglacial water pressure plays a crucial role (Iken & Bindschadler 1986; Jansson 1995; Howat *et al.* 2008; van de Wal *et al.* 2008; Shepherd *et al.* 2009; Bartholomew *et al.* 2010). Consequently, most parameterizations of glacier sliding postulate that there is a relationship between friction, sliding velocity and effective pressure at the glacier bed, where effective pressure is defined as normal stress at the bed minus water pressure (Budd *et al.* 1979). Theory and experiment indicate two primary ways in which effective pressure can affect friction at the base of a glacier. If the bed is composed of a granular material, then a low effective pressure will correspond to weakened grain contacts. This facilitates slip between grains and hence basal ice motion (Iverson *et al.* 1999). Where larger asperities on the bed rather than the strength of subglacial sediments control drag on the base of the glacier, effective pressure controls the degree of contact between ice and bed. At low effective pressure, water-filled cavities can form in the lee of asperities, and their size increases with decreasing effective pressure. Larger cavities correspond to reduced contact, and hence to less drag (Lliboutry 1968; Fowler 1986; Schoof 2005; Gagliardini *et al.* 2007).

In both cases, where friction is controlled by mechanical failure in sediment and by larger asperities, friction increases with effective pressure. In models of glacier and ice sheet dynamics, it can therefore be important to be able to predict effective pressure (see e.g. Flowers *et al.* 2004, 2005; Flowers 2008; Hewitt & Fowler 2008; Pimentel & Flowers 2010). This must be done through a model component that describes the flow of water. There are numerous complications that make this task difficult. While direct observations of the glacier bed are difficult, there is evidence that drainage can generically occur in two distinct styles: through a spatially distributed, effectively porous system that can consist at least in part of the cavities described above, and through a few individual channels (Kamb *et al.* 1985; Iken & Bindschadler 1986; Hubbard *et al.* 1995; Lappegard *et al.* 2006). Modelling the interactions between cavities and channels has been challenging, especially in two dimensions, with recent progress relying on discrete descriptions of channels with prescribed locations coupled either to discrete cavities or a continuum porous model (Schoof 2010; Hewitt 2011).

In addition to the possibility of different styles of drainage, models also have to contend with channels and cavities that may only be partially filled with water, or even with no water at all (see e.g. Fowler 1987, for a discussion). This is most likely when melt water input is low or under thin ice, and is commonly observed near glacier termini. Most current models do not describe partially filled channels and cavities, and instead unphysically predict negative water pressures, a notable exception being the partially filled channel model of Schuler & Fischer (2009). At the opposite extreme, existing models often predict large negative effective pressures in response to increases in water input, corresponding to water pressure significantly exceeding overburden (e.g. Pimentel & Flowers 2010; Schoof 2010). The physics built into these models is however not intended to capture the rapid opening of an ice-water gap that should ensue, which has been modelled as an elastic hydrofracture problem in Tsai & Rice (2010).

In this paper, we consider only a distributed drainage system whose mathematical description is motivated by the dynamics of subglacial cavities. We then focus on the complications introduced by predictions of negative water pressures or negative effective pressures. In particular, we fashion a free boundary model that prevents either situation from occurring, and instead allows for partial filling of the drainage system at zero water pressure (which we refer to as 'underpressure') as well as for the opening of an ice-bed gap at zero effective pressure (or 'overpressure'). In the companion paper (Hewitt *et al.*, 2011, submitted), we then extend the ideas developed here to a model that includes

a description of subglacial channels coupled to the subglacial cavities (see also Hewitt 2011).

The paper is laid out as follows: first, we introduce a continuum description of drainage through subglacial cavities in §2 without considering the complications introduced by under- and overpressure. We contrast this model with previous 'poroelastic' models that are diffusive in character, and show how to compute travelling wave solutions to our model (§3). These solutions can exhibit negative effective pressures at high discharge, and negative water pressures at low discharge. Dismissing these as unphysical, we set about extending the model to account for the basic physics that is likely to apply at under- and overpressure, namely that an air- or vapour-filled gap forms between the top of the water and the cavity roof at sufficiently low water pressure, and that ice and bed separate at zero effective pressure (§4.1). Our description of the latter process is somewhat less sophisticated than the hydrofracture model in Tsai & Rice (2010), and is intended to apply at longer time scales. The advantage of our approach is that it fits naturally into the framework of the continuum drainage model we start out with. The nature of our extended model is that of a free boundary problem that bears some resemblance to bubble cavitation models for negative squeeze films (Ockendon *et al.* 2003) and to Hele-Shaw flows (Howison 1992). In §5, we amend our travelling wave solutions for the extended model, and also show how to compute steady state solutions. We also demonstrate that a numerical method for solving the dynamic extended model described in §4.3 can reproduce the known steady state and travelling wave solutions. Implications of our results as well as differences with alternative models and the need for further model development are discussed in §6.

2. A continuum model for distributed subglacial drainage

Individual cavities form in the lee of asperities on the glacier bed. Ice flows as a viscous gravity current over a typically uneven glacier bed through a combination of shearing and interfacial slip. Where the ice encounters a protrusion on the bed, it is forced upwards, and separates from the bed if the lee side of the protrusion has sufficient curvature. The process can be modelled as a viscous analogue of Hertzian contact with a rigid substrate (Fowler 1986; Kamb 1987; Schoof 2005; Gagliardini *et al.* 2007). Separation between ice and bed first occurs when normal stress attains a critical lower bound at which water or air can force its way between ice and bed, and the lower boundary of the ice is constrained to lie at or above the glacier bed. This approach is suitable for relatively small domains, in which it is feasible to track the contact lines between ice and bed exactly for a known bed geometry.

Our aim is to model a large number of interconnected cavities subject to spatially and temporally varying water pressure. We replace the detailed formulation as a contact problem by a parameterized description of the processes that control cavity size (Walder 1986; Schoof 2010). Individual cavities open due to ice flow at sliding velocity u_b over protrusions of typical height h_r on the glacier bed (figure 1). The size of cavities is limited by the difference between far-field bed normal stress p_i in the ice (which can typically be approximated as hydrostatic) and the water pressure p_w in the cavity. This drives a downward flow of the ice that tends to close the cavity. We assume a power-law rheology for ice (Paterson 1994) that relates strain rate $\mathbf{D}$ to deviatoric stress $\boldsymbol{\tau}$ as $\mathbf{D} = A\tau^{n-1}\boldsymbol{\tau}$ with constant coefficients A and n, where $\tau^2 = \boldsymbol{\tau} : \boldsymbol{\tau}/2$. The cross-sectional area S of the cavity then evolves as a result of differences between opening and closing rates, and we

represent this as

$$\frac{\mathrm{d}S}{\mathrm{d}t} = u_b h_r - A(p_i - p_w)^n l_c(S)^2. \tag{2.1}$$

Here the opening rate $u_b h_r$ is assumed to depend entirely on flow over bedrock roughness, so we are assuming that melting of the overlying ice is insiginificant. This assumption precludes channelization through the mechanism described by Walder (1986), Kamb (1987) and Schoof (2010), which we incorporate into the model in the companion paper (Hewitt, Schoof and Werder, 2011, submitted). l_c is a length scale for viscous closure, which relates the strain rate $A(p_i - p_w)^n$ to the rate of viscous creep closure of the cavity. As a crucial simplification, we assume in formulating (2.1) that this length scale depends only on the current cross-sectional area S of the cavity and no further degrees of freedom describing the specifics of the three-dimensional cavity shape. For now l_c may be seen as a general parameterization (though we will later use $l_c(S)^2 = S$ in numerical solutions); as discussed in greater detail in Schoof (2010), a model of the type (2.1) qualitatively reproduces the behaviour of more sophisticated contact problem models for subglacial cavities.

Importantly, p_i is not the local normal stress at the bed, but far field stress. Hence the quantity

$$N = p_i - p_w \tag{2.2}$$

must be interpreted as a regional effective pressure, which would be the same for any two cavities that are sufficiently close and well-connected to one another to experience the same far field pressure in the ice and the same water pressure. N is *not* a local effective pressure in the sense that it is not the difference between normal stress at the bed and subglacial water pressure: the latter quantity must in fact be zero at the roof of any individual cavity, and varies on the scale of local bed roughness. In fact, its spatial mean over the bed roughness scale equates to our N.

This picture of cavity formation is obviously most appropriate for beds with significant and relatively immobile protrusions. We anticipate that this need not be limited to rigid glacier beds, and that larger rock fragments embedded in granular subglacial sediment can play a role similar to bedrock protrusions. It is less clear if the picture above can be applied to beds composed entirely of fine-grained weak sediments, though the possibility of spontaneous cavity formation on such beds has been considered elsewhere (Schoof 2007*b,a*; Fowler 2009).

Next, we need to convert this description of an individual cavity to a continuum model of cavities on large spatial scales (Hewitt 2011). Instead of tracking individual cavity cross sections S, we homogenize over a representative area of the bed intermediate between the size of individual cavities (whose linear dimensions may be metres or less) and of the glacier as a whole (with a typical length of kilometres or more). As a proxy for cavity size, we define h as the average cavity volume per unit area of the bed. If l_r is a typical spacing between bed protrusions giving rise to cavities, we expect $h = S/l_r$ (or more generally, $h = \bar{S}/l_r$ where $\bar{S}$ is an average cavity size). Consequently (2.1) suggests

$$\frac{\partial h}{\partial t} = u_b h_r/l_r - AN^n \tilde{l}_c(h)^2/l_r. \tag{2.3}$$

More generally, we put

$$\frac{\partial h}{\partial t} = v_o(h) - v_c(N, h) \tag{2.4}$$

where v_o is an opening rate due to flow over asperities, and v_c a closing rate driven by effective pressure $N = p_i - p_w$. In (2.4), we have allowed both opening and closing rates to
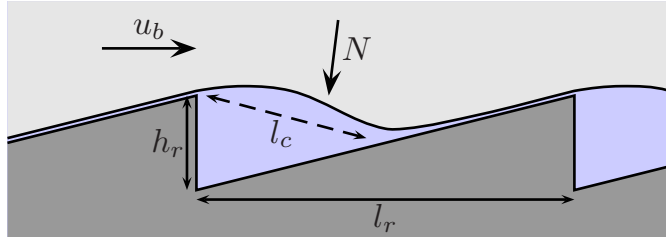
FIGURE 1. A single cavity.

depend on h. Physically, we expect that v_o will eventually decrease with increasing h as larger cavity sizes should lead to less contact between ice and bed protrusions, reducing the tendency to open the cavities further. In particular, h is the mean ice-bed gap size. Unlike what is suggested by (2.3), opening rate should therefore tend to zero when h reaches the roughness scale h_r. Meanwhile v_c depends on h through a viscous length scale $\tilde{l}_c$, which we expect to increase as cavities increase in size, i.e. as h increases. In computational examples we will later use the following two specific forms of v_o and v_c are motivated by (2.3) and that are consistent with the preceeding discussion as well as the work in Schoof (2010) and Hewitt (2011):

$$v_o(h) = u_b(h_r - h)/l_r, \qquad v_c(N, h) = \tilde{A}h|N|^{n-1}N, \tag{2.5}$$

where $\tilde{A}$ is the rheological constant A times a dimensionless factor that depends on the shape of the cavities, and we have assumed that the length scale $\tilde{l}_c$ is simply proportional to h. More generally, our model admits functions v_o and v_c are positive (at least when N is positive), and satisfy

$$\frac{\partial v_c}{\partial h} > 0, \qquad \frac{\partial v_c}{\partial N} > 0, \qquad \frac{\partial v_o}{\partial h} \le 0, \tag{2.6}$$

as well as

$$\lim_{N \downarrow 0} v_c(N, h) = 0, \qquad \lim_{h \uparrow h_r} v_o(h) = 0, \tag{2.7}$$

the last two relations signifying that closure rate goes to zero at vanishing effective pressure, while opening rate does likewise when cavity size reaches the bed roughness scale h_r. In addition, v_o and v_c may also depend explicitly on location through bed roughness parameters like h_r and l_r, while v_o will generally also depend on sliding velocity u_b, which we take to be prescribed in this paper. It is worth pointing out that Hewitt (2011) justifies a model of the form (2.4) for a wider range of physical processes controlling mean ice-bed gap size than the lee-side cavity formation appealed to above, and consequently our model may have wider validity.

We use partial derivatives in (2.4) to signify that $h(x, y, t)$ will in general depend on position as well as time. To close the model (2.4) requires a relationship between N and h. This is supplied by conservation of water: as cavities at the bed change size, water must flow to account for changes in water storage. Water flow in turn depends on water pressure gradients, and hence gradients in effective pressure. Specifically, flow through individual cavities can be related to their cross-sectional size and the hydraulic gradient in the direction of flow. There are two widely used empirical relationships, the Manning (Nye 1976) and Darcy-Weisbach (Clarke 1996) turbulent closure schemes. In the spirit of our continuum model, we homogenize once again over discharge in individual cavities and describe water transport through a two-dimensional flux $\mathbf{q}$ parallel to the glacier bed. Assuming that all cavities are completely filled with water, h can be identified as

the average volume of water stored per unit area of the glacier bed, we have

$$\frac{\partial h}{\partial t} + \nabla \cdot \mathbf{q} = m \qquad (2.8)$$

where m is a prescribed rate of water supply to the bed and ∇ is the two-dimensional divergence operator.

Water flow is driven by gradients of hydraulic potential $\phi(x, y, t)$ at the bed, which we can define as

$$\phi = \rho_w g b + p_w \qquad (2.9)$$

where ρ_w is water density, g acceleration due to gravity, and $b(x, y)$ is the fixed elevation of the bed. Both, a Manning and a Darcy-Weisbach law then motivate a relationship between between water storage h, hydraulic gradient $\nabla \phi$ and flux $\mathbf{q}$ of the form

$$\mathbf{q} = -k h^\alpha \, |\nabla \phi|^{\beta-2} \, \nabla \phi \qquad (2.10)$$

where $\alpha > 1$ and $\beta = 3/2$; our work below will assume only that $\beta > 1$. The formulation proposed in (2.10) differs somewhat from an alternative view of drainage through linked cavities developed principally by Fowler (1987), in that we assume the permeability of the drainage system, and hence discharge, to depend on cavity size h. Naturally, we do not envision all cavities to be the same size. Rather, we suppose that the smallest constrictions, which are likely to control flow, are controlled by the same balance of opening and closing mechanisms as larger cavities, and hence that their size scales with the larger cavities that control water storage. Consequently we assume that discharge and storage can be modelled using the same cavity size variable h. Fowler (1987) by contrast models the connections between cavities as small channels that are kept open not by a balance of opening due to flow over bed roughness and viscous closure as in (2.1), but by a balance between opening due to dissipation-driven melt and viscous closure. We show in appendix A that this mechanism is in fact inconsistent with the idea that water flows in a distributed system that can be modelled as a continuum, and instead leads to the concentration of flow into individual drainage pathways.

Persisting with our model as posed, note that ϕ is related directly to N. We assume that normal stress p_i in the ice at the bed is given in terms of ice thickness through the hydrostatic relation $p_i = \rho_i g(s - b)$, where ρ_i is ice density and $s(x, y)$ is surface elevation of the glacier, which we take to be fixed on timescales over which h changes (typically, drainage systems evolve over timescales of days to weeks or even less, while significant changes in ice geometry usually take years). The definition of N together with (2.9) gives

$$N = \rho_i g s + (\rho_w - \rho_i) g b - \phi. \qquad (2.11)$$

(2.8), (2.10) (2.11) and (2.4) together with suitable boundary conditions then represent a closed model for h and ϕ. Specifically, (2.8), (2.10) and (2.4) together give

$$-\nabla \cdot \left[k h^\alpha |\nabla \phi|^{\beta-2} \nabla \phi \right] + v_o(h) - v_c(N, h) = m \qquad (2.12)$$

With N and ϕ related through (2.11), this is an elliptic problem for ϕ given fixed h that can be solved provided suitable boundary conditions are imposed on ϕ (such as Dirichlet or Neumann conditions), as demonstrated by the convex variational formulation developed later in §4.2. With ϕ computable for given h, (2.4) then determines how h evolves. The model above is somewhat different from poroelastic models in glaciology and elsewhere (Flowers & Clarke 2002). Poroelasticity would correspond to replacing the 'viscous' evolution problem (2.4) by an 'elastic' (i.e., algebraic) relationship between 'pore size' h and effective pressure N.

In much of what follows, we will treat m as a known water input, as is appropriate when the drainage system is forced primarily by melt at the glacier surface (which would be the case for temperate glacier as well as the margins of many ice caps outside the Antarctic during summer). In ice sheets with perennially cold surface conditions such as Antarctica, m may in fact be derived from dissipation of heat by glacier sliding, and could therefore be coupled back to N; we do not consider this scenario here.

Similar models to the above exist in the glaciological literature, notably in Hewitt (2011) and in slightly different form in Creyts & Schoof (2009), while a related discrete model appears in Schoof (2010). Continuum models of this type are usually termed 'sheet models' to distinguish them from models of drainage through individual channels incised into the base of the ice (Röthlisberger 1972; Nye 1976). The connected cavities, which as above can be thought of as two-dimensional pore space, are then referred to as a 'water sheet', and h is the 'sheet thickness'.

Next, we will present travelling wave solutions for the model. These are a particular class of solutions for which the model formulated above is amenable to a semi-analytical treatment. Our aim is to show not only that physically sensible solutions exist, but also to illustrate how the model can predict negative water pressures as well as negative effective pressures. This motivates us to consider how unphysical scenarios generated by these negative pressures can be avoided by changes to the model, and the resulting extended model is then solved numerically.

3. Travelling waves

In this section, we restrict ourselves to one spatial dimension, x, and assume that the bed $b(x)$ and ice surface $s(x)$ are parallel planes inclined downwards in the x-direction. Then the hydraulic gradient $-\nabla\phi$ is simply given by

$$\Psi_0 + \frac{\partial N}{\partial x}$$

where $\Psi_0 = -\rho_w g \partial b/\partial x$ is a positive constant. Flux is then given by

$$q = kh^\alpha \left| \Psi_0 + \frac{\partial N}{\partial x} \right|^{\beta-2} \left(\Psi_0 + \frac{\partial N}{\partial x} \right). \tag{3.1}$$

Next, we seek a travelling wave solution for h and N depending only on $\eta = x - Vt$, joining an upstream flux $q \to q_-$ as $\eta \to -\infty$ to a downstream flux $q \to q_+$ as $\eta \to \infty$. Assuming zero water input m, we have from (2.4) and (2.8)

$$-V\frac{\mathrm{d}h}{\mathrm{d}\eta} + \frac{\mathrm{d}q}{\mathrm{d}\eta} = 0 \tag{3.2}$$

$$-V\frac{\mathrm{d}h}{\mathrm{d}\eta} = v_o(h) - v_c(N, h) \tag{3.3}$$

From (3.2), $q - Vh = q_0$ is a constant. For fixed V and q_0, (3.1) then gives

$$\frac{\mathrm{d}N}{\mathrm{d}\eta} = f(h; q_0, V, \Psi_0) \tag{3.4}$$

where

$$f(h; q_0, V, \Psi_0) = \left| \frac{Vh + q_0}{kh^\alpha} \right|^{(2-\beta)/(\beta-1)} \frac{Vh + q_0}{kh^\alpha} - \Psi_0 \tag{3.5}$$

Together with (3.3) this constitutes a phase plane problem for N and h. The assumption of finite fluxes being attained as $\eta \to \pm\infty$ corresponds to (N, h) approaching fixed points

of the dynamical system (3.3)–(3.4); if these correspond to fluxes q_- and q_+, then h at the fixed points must be given by

$$h_+ = \left(\frac{q_+}{k\Psi_0^{\beta-1}}\right)^{1/\alpha}, \qquad h_- = \left(\frac{q_-}{k\Psi_0^{\beta-1}}\right)^{1/\alpha}. \tag{3.6}$$

Since $q = Vh + q_0$, we find V and q_0 as

$$q_0 = q_+ - Vh_+ = q_- - Vh_-, \qquad V = \frac{q_+ - q_-}{h_+ - h_-}, \tag{3.7}$$

respectively. As $h_\pm$ increases with $q_\pm$, it follows that the pattern velocity V is positive. The wave moves downslope.

The corresponding effective pressures N_+ and N_- are determined implicitly through

$$v_o(h_\pm) - v_c(N_\pm, h_\pm) = 0, \tag{3.8}$$

where the constraints (2.6) and (2.7) ensure that solutions are unique and that $N_\pm$ decreases monotonically with increasing $h_\pm$. In our numerical examples, we use the forms of v_o and v_c in (2.5). For these, (3.8) can in fact be solved explicitly to give

$$N_\pm = \left|\frac{u_b(h_r - h_\pm)}{\tilde{A}l_r h_\pm}\right|^{-1+1/n} \frac{u_b(h_r - h_\pm)}{\tilde{A}l_r h_\pm}. \tag{3.9}$$

The solution to (3.3)–(3.4) must approach the fixed points $(h_\pm, N_\pm)$ as $\eta \to \pm\infty$. The stability properties of the fixed points can be determined from the Jacobian of the dynamical system,

$$J = \begin{pmatrix} (v_{c,h} - v_{o,h})/V & v_{c,N}/V \\ f_h & 0 \end{pmatrix} \tag{3.10}$$

where $v_{o,h}$, $v_{c,h}$, $v_{c,N}$ and f_h are the partial derivatives of v_o, v_c and f with respect to the variable indicated, evaluated at the fixed point. Eigenvalues of J are

$$\lambda = (v_{c,h} - v_{o,h})/(2V) \pm \sqrt{(v_{c,h} - v_{o,h})^2/(4V^2) + f_h v_{c,N}/V}, \tag{3.11}$$

and trajectories near the fixed point behave as $(h - h_\pm)$, $(N - N_\pm) \sim \exp(\lambda\eta)$. With the constraints in (2.6), one eigenvalue always has positive real part, which ensures that trajectories can reach the fixed point at $\eta = -\infty$. To reach the fixed point at $+\infty$ requires an eigenvalue with negative real part. In fact, this implies a positive and a negative real eigenvalue, so that the fixed point must be a saddle and the orbit into it is unique (and therefore so is the travelling wave solution, up to a shift in η). A negative eigenvalue in turn requires $f_h > 0$. Differentiation, some algebra and use of the mean value theorem as well as (3.6) shows that $f_h(h_+)$ has the same sign as

$$h_+ V - \alpha q_+ = \frac{h_+(q_+ - q_-)}{h_+ - h_-} - \alpha q_+ \tag{3.12}$$

$$= \alpha k\Psi_0^{\beta-1} h_+ [h_m^{\alpha-1} - h_+^{\alpha-1}] \tag{3.13}$$

where h_m is some value intermediate between h_+ and h_-. Positive f_h is equivalent to $h_+ < h_m$, and it follows that $h_+ < h_-$: the travelling wave has a thicker h upstream and thinner h downstream (and therefore larger flux upstream than downstream, $q_- > q_+$). It can similarly be shown that $f_h(h_-)$ is then negative, so that the eigenvalues for (h_-, N_-) both have positive real parts, so the upstream fixed point is an unstable centre or spiral. This leads to an orbit connecting (h_-, N_-) to (h_+, N_+) as indicated in figure 2.

A few solutions using (2.5) are shown in figure 2. The crucial observation here is
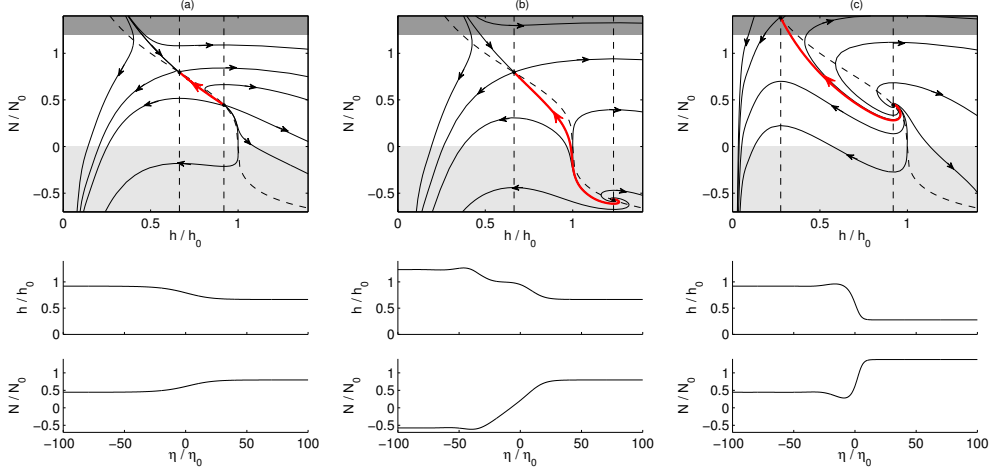
FIGURE 2. Travelling wave solutions. In these computations, we have used (2.5), and scaled the variables with $h_0 = h_r$, $q_0 = kh_r^\alpha \Psi_0^{\beta-1}$, $N_0 = (u_b/\tilde{A}l_r)^{1/n}$, $\eta_0 = N_0/\Psi_0$, $V_0 = q_0/h_0$. We then have a three-parameter family of solutions, determined solely by the scaled upstream and downstream fluxes q_+ and q_- and the length scale ratio $\varepsilon = u_b\eta_0/(V_0 l_r)$. Here we have put $\varepsilon = 0.25$. In each column, the top panel shows the phase plane, the bottom panel shows the actual travelling wave solutions $h(\eta)$ and $N(\eta)$. In each phase portrait, the dashed lines are nullclines, while the thick orbit (shown in red in the electronic version) is the unique orbit connecting the two fixed points. The light grey and dark grey shaded regions represent $N < 0$ and $N > p_i$, where we have arbitrarily set $p_i = 1.2N_0$ here. The left-hand column ($q_- = 0.9q_0$ and $q_+ = 0.6q_0$) corresponds to a physically acceptable solution, in which N never becomes negative or exceeds the ice overburden p_i. The middle column ($q_- = 1.3q_0$ and $q_+ = 0.3q_0$) shows a solution in which effective pressure becomes negative and gap width h exceeds the roughness scale h_r sufficiently far upstream. The right-hand column ($q_- = 0.9q_0$ and $q_+ = 0.2q_0$) shows a solution for which $N > p_i$ sufficiently far downstream.

that, while physically acceptable solutions are clearly possible, it is also possible to find situations in which $N < 0$ (column (b)). The model in §2 is not intended for this situation as it is unlikely that water pressure exceeding ice pressure would simply lead to a steady opening of cavities that are spatially confined: instead, we expect water to leak laterally out of the cavities, causing ice and bed to separate everywhere. The solution is also clearly unphysical as the resulting negative closure rate v_c must be balanced by a negative opening rate v_o, which (2.5) permits mathematically when $h > h_r$, but which is physical nonsense: when $h > h_r$, there is no ice-bed contact and hence interactions with bed roughness no longer have an impact on the mean ice-bed gap h. Physically, negative effective pressures are predicted when the upstream flux q_- is too large, requiring a gap width $h_- = (q_-/k\Psi_0^{\beta-1})^{1/\alpha}$ that exceeds the roughness scale h_r.

More subtly, it is also possible to find solutions for which water pressure p_w is negative (column (c)). This problem is not immediately obvious above because $p_w = p_i - N$, and $p_i = \rho g(s - b)$ does not feature explicitly in the travelling wave problem (3.3)–(3.4). However, for a given p_i, negative p_w arises whenever the downstream flux q_+ is sufficiently small that the thickness $h_+ = (q_+/k\Psi_0^{\beta-1})^{1/\alpha}$ can only be maintained by effective presssures N that exceed ice pressure p_i. Again, this situation is unphysical; instead of attaining negative water pressures, we expect water vapour to form or air to enter into the gap between ice and bed if there is a connection with the atmosphere.
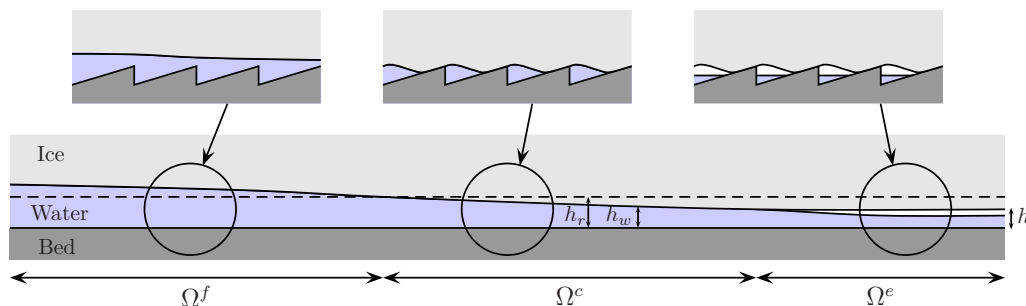
FIGURE 3. The partitioning of the domain Ω into Ω^e, Ω^f and Ω^c. Here h_r denotes the height of bed bumps, h is the mean void space height between ice and bed (averages over the bed roughness scale shown in the inset images), and h_w is the mean water depth at the bed, likewise averaged.

4. Over- and underpressure: a free boundary problem

4.1. *Model Formulation*

The physics included in the model in §2 does not apply straightforwardly when zero water pressure p_w or zero effective pressure N is reached (which we refer to as 'underpressure' and 'overpressure', respectively, while regions in which N and p_w are both positive are referred to as having 'normal pressure'). The model also cannot correctly capture complete separation of ice and bed, which we have seen above in association with overpressure. Alternative descriptions must be sought for these cases. In addition, the regions where over- and underpressure occur are not known *a priori* but can evolve with time. We formulate a free boundary problem to capture the relevant physics below.

Negative water pressure $p_w < 0$ is impossible. Instead, we expect separation between water and the ice roof of the cavities, with the space between being occupied either by water vapour or air. We do not distinguish between these two cases and assume instead that water-ice separation occurs when water pressure drops to zero. Presumably, voids between water and ice roof will typically be filled with a mixture of vapour and air at atmospheric pressure, and pure water vapour is only likely to be present where there are no connections through cracks to the atmosphere at all.

The possibility of only partially water-filled cavities forces us to distinguish between mean ice-bed gap size $h(x, y, t)$ and water level $h_w(x, y, t)$, where $h_w \le h$. Given a domain $\Omega \subset \mathbb{R}^2$, we can then identify the regions of partially-filled cavities as (see figure 3)

$$\Omega^e(t) = \{(x, y) \in \Omega : h_w(x, y, t) < h(x, y, t)\}. \tag{4.1}$$

By assumption we have $p_w = 0$ on Ω^e . Defining

$$\phi_m(x, y) = \rho_w g b(x, y), \tag{4.2}$$

this implies a prescribed hydraulic potential

$$\phi = \phi_m \qquad \text{on } \Omega^e. \tag{4.3}$$

As the mean ice-bed gap h no longer reflects water levels everywhere in the domain, (2.10) needs to be re-written as

$$\mathbf{q} = -k h_w^\alpha \left| \nabla \phi \right|^{\beta - 2} \nabla \phi \tag{4.4}$$

and likewise mass conservation has to be re-written, yielding

$$\frac{\partial h_w}{\partial t} - \nabla \cdot \left[k h_w^\alpha \left| \nabla \phi \right|^{\beta - 2} \nabla \phi \right] = m \qquad \text{on } \Omega, \tag{4.5}$$

This holds on the entire domain Ω, not only on Ω^e. However, with ϕ given by (4.3) on Ω^e, (4.5) can be recognised as a hyperbolic problem for h_w on this sub-domain: we have a variant of Burgers' equation in two spatial dimensions. Following ice-water separation, h_w and h can evolve independently until h_w increases sufficiently to completely fill the gap again. In Ω^e, h still evolves according to the balance of gap opening and viscous closure, and satisfies (2.4),

$$\frac{\partial h}{\partial t} = v_o(h) - v_c(N, h) \qquad \text{on } \Omega^e. \tag{4.6}$$

Similarly, we can identify regions where there is complete separation of ice and bed as

$$\Omega^f(t) = \{(x, y) \in \Omega : h(x, y, t) > h_r(x, y)\}. \tag{4.7}$$

One can conceive of water pressure p_w exceeding overburden p_i by a finite amount on Ω^f. However the length scale associated with viscous deformation driven by the then negative effective pressure would be comparable with the linear dimensions of Ω^f and therefore, by assumption in our continuum model, much larger than the scale of an individual cavity. The rate of gap opening should then be much larger than typical values of v_c, and therefore large compared with the rates of change of h one would expect. Consequently, we assume that insignificant departures from overburden are required to drive the opening and closing of the ice-water gap in Ω^f. Consequently, we set $p_w = p_i$, and the ice in Ω^f is essentially afloat. This may be violated in exceptional circumstances when the scale argument above fails, for instance when the rapid input of large amounts of water demands high opening rates that can only be accommodated by negative effective pressures. The abrupt drainage of surface lakes to the glacier bed is a situation in which this is likely to be the case (Das *et al.* 2008). In that case, it may also be necessary to take account of the viscoelastic behaviour of ice at short time scales. A more classical hydrofracture model may then be required, as presented in Tsai & Rice (2010).

Here we do not consider this scenario. Defining

$$\phi_0(x, y) = \rho_i g s + (\rho_w - \rho_i) g b, \tag{4.8}$$

(2.11) then allows us to write

$$\phi = \phi_0 \qquad \text{on } \Omega^f. \tag{4.9}$$

Note that $\phi_0 > \phi_m$ whenever the glacier thickness $s - b > 0$; complete separation and partially filled cavities can obviously not occur simultaneously. Water completely fills the ice-bed gap, whose width is controlled not by the difference of opening and closing rates, but by mass conservation for water. Hence

$$h = h_w \qquad \text{on } \Omega^f, \tag{4.10}$$

where h_w is once more determined by (4.5). With ϕ constrained by (4.9), we again have the same Burgers-type equation as before. Note that, to preclude unphysical pooling of water, we assume here that neither ϕ_0 nor ϕ_m has any local minima within the domain; the changes to the model necessary to allow minima of ϕ_0 (locations where subglacial lakes can form) will be dealt with in the companion paper (Hewitt *et al.*, 2011, submitted).

This leaves the region where we have neither separation between water and ice, nor complete separation between ice and bed. We label this as

$$\Omega^c = \Omega \setminus (\Omega^f \cup \Omega^e). \tag{4.11}$$

In this region as in Ω^f, cavities are completely filled and therefore

$$h_w = h \leq h_r, \tag{4.12}$$

where h_w again evolves according to (4.5). On Ω^c, it is possible for water pressure as well as effective pressure to be positive, as implicitly intended in §2. We label these parts of Ω^c as Ω^c_0. Here the original model of §2 applies:

$$\phi_m < \phi < \phi_0, \qquad \frac{\partial h_w}{\partial t} = \frac{\partial h}{\partial t} = v_o(h) - v_c(N, h) \qquad \text{on } \Omega^c_0. \qquad (4.13)$$

There is also the possibility that (4.12) is satisfied but one of the bounds in (4.13) is reached. Take first the incipient underpressure case, corresponding to $p_w = 0$. We label regions in Ω^c where this applies by Ω^c_-. This is the situation in which water-ice separation may be about to occur, and lower water pressures are not possible. It must therefore correspond to $h - h_w$ either remaining at zero or becoming positive, where h evolves according to the difference between opening and closing rates:

$$\phi = \phi_m, \qquad \frac{\partial h_w}{\partial t} \leq \frac{\partial h}{\partial t} = v_o(h) - v_c(N, h) \qquad \text{on } \Omega^c_-. \qquad (4.14)$$

Naturally, parts of Ω^c_- may no longer be part of $\Omega^c(t)$ after a finite time, but we have to allow for the possibility that (4.14) holds in order to identify those regions where separation is about to occur.

Lastly, there is the possibility that the overpressure case $N \leq 0$ is attained in Ω^c. We label regions where this occurs by Ω^c_+. By analogy with Ω^f, we assume that the ice-bed can open at whatever rate conservation of water demands with only a negligible amount of overpressure. We model this by requiring that N in fact remains non-negative and imposing that at $N = 0$, the net opening rate of the ice-bed gap can exceed that predicted by (4.13) in such a way as to maintain $h = h_w$. Hence

$$\phi = \phi_0, \qquad \frac{\partial h_w}{\partial t} = \frac{\partial h}{\partial t} \geq v_o(h) - v_c(N, h) \qquad \text{on } \Omega^c_+, \qquad (4.15)$$

where naturally the closure rate $v_c(N, h) = 0$ as $N = 0$, but we retain it for later convenience.

We will show in §4.2 how (4.13)–(4.15) combined with (4.5) constitute a well-posed problem for ϕ. We still need to consider jump conditions at interior boundaries between the sub-domains Ω^e, Ω^c and Ω^f, and specify boundary conditions at the exterior boundary $\partial\Omega$ of the domain.

At boundaries between the sub-domains, we assume that water pressure p_w and hence hydraulic potential ϕ is continuous. Since ϕ is prescribed in Ω^e and Ω^f, this amounts to prescribing $\phi = \phi_0$ at boundaries between Ω^f and Ω^c, and $\phi = \phi_m$ at boundaries with Ω^e. In addition, we require that water be conserved at boundaries between the sub-domains, which amounts to interpreting (4.5) in weak form throughout the domain. As we shall show below in §5.1, shocks are possible not only within Ω^e and Ω^f (where one would expect them as (4.5) is hyperbolic there) but also at the boundaries of Ω^c.

Boundary conditions must also be specified on the exterior boundary of Ω. This is somewhat delicate as the type of boundary condition that can be applied is restricted by whether the exterior boundary borders Ω^f, Ω^e or the different parts of Ω^c, and these subdomains are not known *a priori* and can furthermore change over time. For instance, on Ω^c_0, the original model of §2 holds. This requires boundary conditions on ϕ to solve the elliptic problem (2.12), while (2.4) needs only initial conditions on h but no boundary conditions. Boundaries bordering Ω^c_0, can therefore accept Dirichlet or Neumann conditions on ϕ. For boundaries of Ω^f, Ω^c_+, Ω^c_- and Ω^e, prescribed fluxes are needed on inflow boundaries as Cauchy conditions on h for the hyperbolic problem (4.5), while flux cannot be prescribed on outflow boundaries. The Cauchy conditions for h on inflow boundaries therefore take the same form as Neumann conditions on ϕ, and such prescribed flux
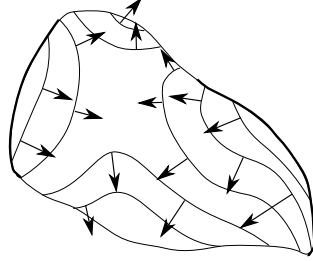
FIGURE 4. Identification of inflow and outflow boundaries. Contour lines of ϕ_0 (or ϕ_m) are shown with arrows pointing from high ϕ_0 to low ϕ_0. The parts of the boundary marked as thick curves are then ϕ_0- (or ϕ_m-) inflow boundaries, while the remaining parts are ϕ_0- (or ϕ_m-) outflow boundaries.

conditions are therefore the obvious conditions to impose on possible inflow boundaries when it is unclear which type of subdomain these boundaries will correspond to. The outflow boundaries, while requiring no conditions on h, can however still correspond to Dirichlet conditions on ϕ in the form $\phi = \phi_0$ or $\phi = \phi_m$. We expect every part of $\partial\Omega$ should have either a pressure or a flux condition applied to close the problem (as this was the case in the original model of §2), and hence Dirichlet conditions are obvious conditions to prescribe on possible outflow boundaries.

Here we make the following choice that should always lead to a well-posed problem. We begin by identifying possible outflow boundaries for over- and underpressured conditions (which we call ϕ_0- and ϕ_m-outflow boundaries) as those parts of $\partial\Omega$ on which $\nabla\phi_0$ and $\nabla\phi_m$ have negative normal components, respectively, and likewise identify natural inflow boundaries where they have positive normal components (figure 4). Next, we split the boundary $\partial\Omega$ into two disjoint parts $\partial\Omega_N$ and $\partial\Omega_D$, which need not correspond to the identified inflow and outflow boundaries in any specific way. On $\partial\Omega_D$, we apply Dirichlet conditions that satisfy the constraint $\phi_m \leq \phi \leq \phi_0$, but demand that the limiting cases $\phi = \phi_0$ and $\phi = \phi_m$ can only hold at the corresponding outflow boundaries, and not on their inflow counterparts. This should prevent missing Cauchy conditions on h for (4.5) at inflow boundaries. On $\partial\Omega_N$, we apply prescribed flux conditions. However, we have to bear in mind that it will not be possible to prescribe arbitrary inflow on ϕ_0-outflow boundaries; in particular, once overpressure is reached on these boundaries, only outflow is possible. To deal with this, we define a rate of inflow $q_n > 0$ along $\partial\Omega_N$. On parts of $\partial\Omega_N$ that are ϕ_0-inflow boundaries, we are always at liberty to enforce inflow q_n:

$$-kh_w^\alpha \left|\nabla\phi\right|^{\beta-2} \nabla\phi \cdot \mathbf{n} = -q_n, \qquad (4.16a)$$

where $\mathbf{n}$ is the outward-pointing unit normal. On parts that are ϕ_0-outflow boundaries, we need the more complicated

$$-kh_w^\alpha \left|\nabla\phi\right|^{\beta-2} \nabla\phi \cdot \mathbf{n} = -q_n \qquad \text{if } \phi_m \leq \phi < \phi_0, \qquad (4.16b)$$

$$-kh_w^\alpha \left|\nabla\phi\right|^{\beta-2} \nabla\phi \cdot \mathbf{n} \geq -q_n \qquad \text{if } \phi = \phi_0. \qquad (4.16c)$$

Physically, the inequality in (4.16c) allows arbitrary flux coming out of ϕ_0-outflow boundaries when overpressure is reached. (Presumably there is no analogous problem to deal with for the $\phi = \phi_m$ case: at ϕ_m-outflow boundaries bordering Ω^e or Ω_-^C, it should be possible to accommodate specified inflow q_n by filling the water-ice gap completely so a shock can propagate into the domain. That part of the boundary will then no longer border Ω^e or Ω_-^c after any finite amount of time.) We note that the boundary conditions (4.16) are actually not Neumann conditions on ϕ *per se* in the mathematical sense, but

are of similar form to the mixed boundary conditions that are applied in Signorini-type elastic contact problems (Kikuchi & Oden 1988).

As an example of physically sensible conditions compatible with the above, put $\phi = \phi_m$ on all parts of the glacier margin that are ϕ_m-outflow boundaries: water pressure is then atmospheric there. At inflow boundaries, flux into the domain can be specified instead as described above. When q_n is small enough, the model will naturally predict $\phi = \phi_m$ at the boundary (see the solutions in 5.2 below). If q_n becomes larger, this may require $\phi > \phi_m$, which corresponds physically to some pooling of water at the margin. It is possible that more elaborate boundary conditions may be required in practice depending on glacier geometry and the physics of the glacier margin; here we persist with the above for simplicity.

4.2. *Determination of ϕ: an obstacle problem*

It is not immediately obvious that (4.13)–(4.15) lead to a well-posed model for ϕ in Ω^c. We proceed to demonstrate this here by means of a variational formulation, which also leads directly to a numerical method of solution. Combining (4.13)–(4.15) with (4.5) leads to the conclusion that on any part of Ω^c, one of the following three cases must apply:

$$\phi_m < \phi < \phi_0 \quad \text{and} \quad -\nabla \cdot \left[kh^\alpha \left| \nabla \phi \right|^{\beta-2} \nabla \phi \right] + v_o(h) - v_c(h, N) - m = 0, \quad (4.17a)$$

$$\phi = \phi_0 \quad \text{and} \quad -\nabla \cdot \left[kh^\alpha \left| \nabla \phi \right|^{\beta-2} \nabla \phi \right] + v_o(h) - v_c(h, N) - m \leq 0, \quad (4.17b)$$

$$\phi = \phi_m \quad \text{and} \quad -\nabla \cdot \left[kh^\alpha \left| \nabla \phi \right|^{\beta-2} \nabla \phi \right] + v_o(h) - v_c(h, N) - m \geq 0. \quad (4.17c)$$

However, we do not know *a priori* where each of these cases applies: the regions Ω^c_+, Ω^c_0 and Ω^c_- must be found as part of the solution. For fixed h (i.e., at a fixed point in time), this takes the mathematical form of a so-called obstacle problem (see e.g. Kinderlehrer & Stampacchia 1980; Kikuchi & Oden 1988; Evans 1998): the inequality constraints in this problem determine implicitly where each of the cases listed occurs.

A variational formulation can be obtained by picking a test function θ that satisfies the same inequality constraints as ϕ,

$$\phi_m \leq \theta \leq \phi_0 \tag{4.18}$$

and multiplying the second relation for each case in (4.17) by $\theta - \phi$. Making use of the first relation in each case as well as of the constraints on θ leads to

$$(\theta - \phi) \left\{ -\nabla \cdot \left[kh_w^\alpha \left| \nabla \phi \right|^{\beta-2} \nabla \phi \right] + v_o(h) - v_c(h, N) - m \right\} \geq 0 \tag{4.19}$$

everywhere on Ω^c. Integrating by parts over Ω^c, we have the weak form

$$\int_{\Omega^c} kh^\alpha \left| \nabla \phi \right|^{\beta-2} \nabla \phi \cdot \nabla(\theta - \phi) - v_c(h, N)(\theta - \phi) - [m - v_o(h)](\theta - \phi) \, \mathrm{d}\Omega$$

$$- \int_{\partial \Omega^c} (\theta - \phi) kh^\alpha \left| \nabla \phi \right|^{\beta-2} \nabla \phi \cdot \mathbf{n} \, \mathrm{d}\Gamma \geq 0 \tag{4.20}$$

where $\mathbf{n}$ is the outward-pointing unit normal to the boundary $\partial \Omega^c$. If we assume additionally that θ satisfies the same Dirichlet conditions as ϕ, then the boundary integral can be simplified further. On any part of $\partial \Omega^c$ that is interior to Ω, we have prescribed ϕ from the adjacent part of Ω, which can be either Ω^f (so $\theta = \phi = \phi_0$) or Ω^e (so $\theta = \phi = \phi_m$). The boundary integral therefore vanishes on those parts. This leaves only parts of $\partial \Omega^c$

that are also exterior boundaries to Ω, and from (4.16), we get

$$\int_{\Omega^c} kh^\alpha \left|\nabla\phi\right|^{\beta-2} \nabla\phi \cdot \nabla(\theta - \phi) - v_c(h, N)(\theta - \phi) - [m - v_o(h)](\theta - \phi)\,\mathrm{d}\Omega$$

$$- \int_{\partial\Omega^c \cap \partial\Omega_N} q_n(\theta - \phi)\,\mathrm{d}\Gamma \geq 0 \quad (4.21)$$

This variational inequality must hold for any test function θ that satisfies the relevant constraints. Similar variational equalities occur not only in elasticity theory but also in the much more closely related problem of bubble cavitation (e.g. Kinderlehrer & Stampacchia 1980).

Given the constraints on v_c in (2.6) and the definition of N in terms of ϕ in (2.11), standard methods in convex analysis (e.g. Ekeland & Temam 1976) show that the variational inequality (4.21) is in fact equivalent to a minimization principle. We define the following antiderivative of v_c:

$$\Lambda(\phi; h) := \int_0^{\phi_0 - \phi} v_c(N', h)\,\mathrm{d}N'. \quad (4.22)$$

As v_c is an increasing function of N by (2.6), Λ is convex in ϕ. For fixed h, solutions ϕ to (4.21) then minimize the functional

$$J(\phi) := \int_{\Omega^c} \frac{1}{\beta} kh^\alpha \left|\nabla\phi\right|^\beta + \Lambda(\phi; h) - [m - v_o(h)]\phi\,\mathrm{d}\Omega - \int_{\partial\Omega^c \cap \partial\Omega_N} q_n\phi\,\mathrm{d}\Gamma \quad (4.23)$$

subject to the constraint that $\phi_m \leq \phi \leq \phi_0$ as well as the applied Dirichlet conditions. Technically, we should specify that J is defined on the function space $W^{1,\beta}(\Omega^c)$. The minimization problem is then well-posed (in the sense of having a unique weak solution that changes continuously with the forcing functions) subject to mild constraints on Ω^c, h and the functions v_c and v_o as well as on the forcing terms m and q_n. For instance, it suffices that Ω^c is bounded with a Lipschitz boundary, while $h \in L^\infty(\Omega^c)$ with $h \geq h_0 > 0$ for some constant h_0 almost everywhere in Ω^c, that ϕ_m, $\phi_0 \in L^\infty(\Omega^c) \cap W^{1,\beta}(\Omega^c)$, while m, $v_o(h) \in L^{\beta/(\beta-1)}(\Omega^c)$, $q_n \in L^{\beta/(\beta-1)}(\partial\Omega)$, and Λ is a strictly convex, increasing function of its first argument with $\Lambda(\phi_0, h) = 0$, such that $\Lambda(\phi, h)$ is measurable for every $\phi \in L^\beta(\Omega^c)$ with $\int_\Omega \Lambda(\phi_m, h)\,\mathrm{d}\Omega$ finite.

Not only does the minimization problem for (4.23) allow us to see that the problem for ϕ is well-posed, it also provides a numerical method through the application of minimization techniques. We exploit this below.

4.3. *Numerical solution algorithm*

The model can be summed up as follows: At any time t, the domain Ω can be divided into three disjoint subdomains Ω^e, Ω^f and Ω^c defined through (4.1), (4.7) and (4.11). On Ω^e, $\phi = \phi_m$, on Ω^f, $\phi = \phi_0$ while on Ω^c, ϕ is determined by minimizing the functional J defined in (4.23) subject to the constraints $\phi_m \leq \phi \leq \phi_0$ as well as continuity of ϕ at boundaries with Ω^e and Ω^f, and compliance with any Dirichlet conditions imposed on the boundary $\partial\Omega$ of the domain. h_w evolves throughout Ω according to (4.5), which must be understood in weak form and requires appropriate Cauchy boundary conditions in the form of prescribed fluxes on the relevant parts of the bounary. h is constrained to remain equal to h_w everywhere except those parts of the domain where $\phi = \phi_m$, which we labelled $\Omega^e \cup \Omega^c_-$ above. Here h evolves independently of h_w according to (2.4).

We have implemented the following operator-splitting approach to solving this problem numerically:

- For fixed h and h_w, calculate ϕ:

(a) Divide domain into the three regions Ω^e, Ω^f and Ω^c.

(b) On Ω^e, assign $\phi = \phi_m$.

(c) On Ω^f, assign $\phi = \phi_0$.

(d) On Ω^c, find ϕ by minimizing J, subject to $\phi_m \leq \phi \leq \phi_0$ and applied Dirichlet conditions.

- Given ϕ, update h and h_w:

(e) Based on the computed ϕ and current values of h and h_w, divide the domain into three new regions, $\Omega^+ = \Omega^f \cup \Omega^c_+$, $\Omega^- = \Omega^e \cup \Omega^c_-$, $\Omega^0 = \Omega^c_0$.

(f) On Ω^0, step h forward in time using (2.4), and set $h_w = h$. This should be equivalent to solving (4.5) for h_w, and setting $h = h_w$, but for realistic parameter choices, the latter problem can be stiff. $\partial h_w/\partial t$ in (4.5) is then typically much smaller than the other two terms, so even a small error in ϕ can generate a significant error in $\partial h/\partial t$ computed from (4.5); in that case, it is preferable to evolve h through (2.4)

(g) On Ω^+, step h_w forward using (4.5), and set $h = h_w$.

(h) On Ω^-, step h_w forward using (4.5) and step h forward using (4.6).

(i) Some post-processing may be required in Ω^e, where the updated values of h_w and h may not satisfy $h_w \leq h$. Where this is violated, we set $h_w = h$, and adjust the fluxes in (4.5) to move the excess mass into the neighbouring empty region. Regions where this happens will be treated as parts of Ω^c for the next calculation of ϕ.

Spatial discretization is through a mixed finite element / finite volume scheme, and we have so far focused on implementation in one spatial dimension. ϕ is solved for using piecewise linear finite elements, while time stepping for h and h_w uses a finite volume scheme defined on the reciprocal mesh: the nodes of the finite element mesh where ϕ is solved for are also cell centres at which h and h_w are computed. An element in the finite element mesh is identified as lying in Ω^c if $h_w = h < h_r$ at all of its vertices, and as being part of Ω^e or Ω^f otherwise. Finite volume cells are assigned to Ω^+, Ω^0 and Ω^- based on the values of ϕ at their centres.

Dirichlet conditions on ϕ are applied at those nodes of Ω_c that border parts of Ω^f and Ω^e, thus marking the boundary with either Ω^e or Ω^f, and at nodes that lie on the relevant parts $\partial\Omega_D$ of the boundary of the domain. ϕ is then found by minimizing the discrete version of J in (4.23) using an augmented Lagrangian algorithm to handle both the p-Laplacian nonlinearity and the inequality constraints on ϕ (Glowinski 1984, chapter 6).

An explicit time step is employed to evolve h and h_w. A first-order accurate upwind scheme based on the computed values of ϕ is used to solve (4.5), while (2.4) takes the form of a local ordinary differential equation and involves no flux computation. A subtlety arises at the boundary between Ω^0 and Ω^+ or Ω^-, because the different discretisations required for the finite volume and finite element calculations, as well as the necessity to discretize the boundary itself, mean that the change in h_w does not always agree with the change in h when it should (that is, on finite volume cells that lie in Ω^0 but border cells in Ω^+ or Ω^-). To ensure that mass is conserved in those cases, when the computed h_w is larger than h, we add the excess mass $h_w - h$ to the neighbouring cells in Ω^+ or Ω^-; this method also accounts for step (i) in the above procedure.

We have been able to apply the algorithm above to a variety of model scenarios, but to test its performance, we will compare its output only to two particular classes of solutions below that can be computed by alternative means and therefore provide a means of benchmarking. The first of these is the travelling wave solutions of §3, which must be adapted to over- and underpressure. These provide a useful benchmark as our numerical solutions is based on a fixed mesh, and travelling waves provide a time-dependent test case. The second class of solutions consists of steady state solutions for finite glacier

lengths. The steady state solutions in particular also provide physical insight into conditions under which over- and underpressure may be expected under glaciers.

5. Solutions

5.1. *Travelling waves revisited*

The travelling wave solutions of §3 can be extended to the case of over- and underpressure. We consider two cases: one in which an overpressured region upstream connects to a region that is neither over- nor underpressured below (to which we refer as being 'normally-pressured'), and one in which a normally-pressured region lies upstream of an underpressured region (these two cases correspond to the unphysical examples (b) and (c) in figure 2). We then test whether the method in §4.3 can reproduce these travelling wave solutions.

Denoting the travelling wave coordinate again by $\eta = x - Vt$, (4.5) becomes

$$-V\frac{\mathrm{d}h_w}{\mathrm{d}\eta} + \frac{\mathrm{d}q}{\mathrm{d}\eta} = 0, \tag{5.1}$$

which must hold throughout the domain. Again, we conclude that

$$q - Vh_w = q_0 \tag{5.2}$$

where q_0 is a constant. This holds across shocks, where q and h_w both change discontinuously: the shock travels at a Rankine-Hugoniot velocity equal to the the pattern velocity, since $[q]_-^+/[h_w]_-^+ = V$, where $[\cdot]_-^+$ denotes the jump in the bracketed quantity across the shock. (4.4) can once more be re-written as

$$\frac{\mathrm{d}N}{\mathrm{d}\eta} = f(h_w; q_0, V, \Psi_0), \tag{5.3}$$

where the functional form of f is still given by (3.5). We again seek a travelling wave solution that connects an upstream flux q_- to a downstream flux q_+, with associated water levels h_{w-} and h_{w-} defined analogously to (3.6):

$$h_{w+} = \left(\frac{q_+}{k\Psi_0^{\beta-1}}\right)^{1/\alpha}, \qquad h_{w-} = \left(\frac{q_-}{k\Psi_0^{\beta-1}}\right)^{1/\alpha}, \tag{5.4}$$

and the pattern velocity is

$$V = (q_+ - q_-)/(h_{w+} - h_{w-}). \tag{5.5}$$

Next, consider the specific case of an overpressured region upstream of a normally-pressured region, with the boundary between the two at $\eta = 0$. In the overpressured region, we have a constant solution

$$h = h_w = h_{w-} > h_r, \qquad N = 0, \qquad \text{for } \eta < 0, \tag{5.6}$$

In the normally-pressured region $\eta > 0$, we have $h_w = h$, and the original travelling wave model (3.3) and (3.4) holds, with (h, N) approaching the fixed point $(h_+, N_+) = (h_{w+}, N_+)$ as $\eta \to +\infty$. The results in §3 show that there is a unique orbit into this fixed point as $h_{w+} < h_r < h_{w-}$. All we have to do is trace this orbit back to the first point where $N = 0$, which marks the boundary $\eta = 0$ with the overpressured region. (It is straightforward to show from $v_c(h, N) = v_o(h) + V\,\mathrm{d}h/\mathrm{d}\eta$ that h can only approach h_r from below if simultaneously $N \to 0$, so $h = h_r$ cannot occur at an earlier point.) The solution generally has a shock at $\eta = 0$, with $h = h_{w-} > h_r$ upstream and $h < h_r$
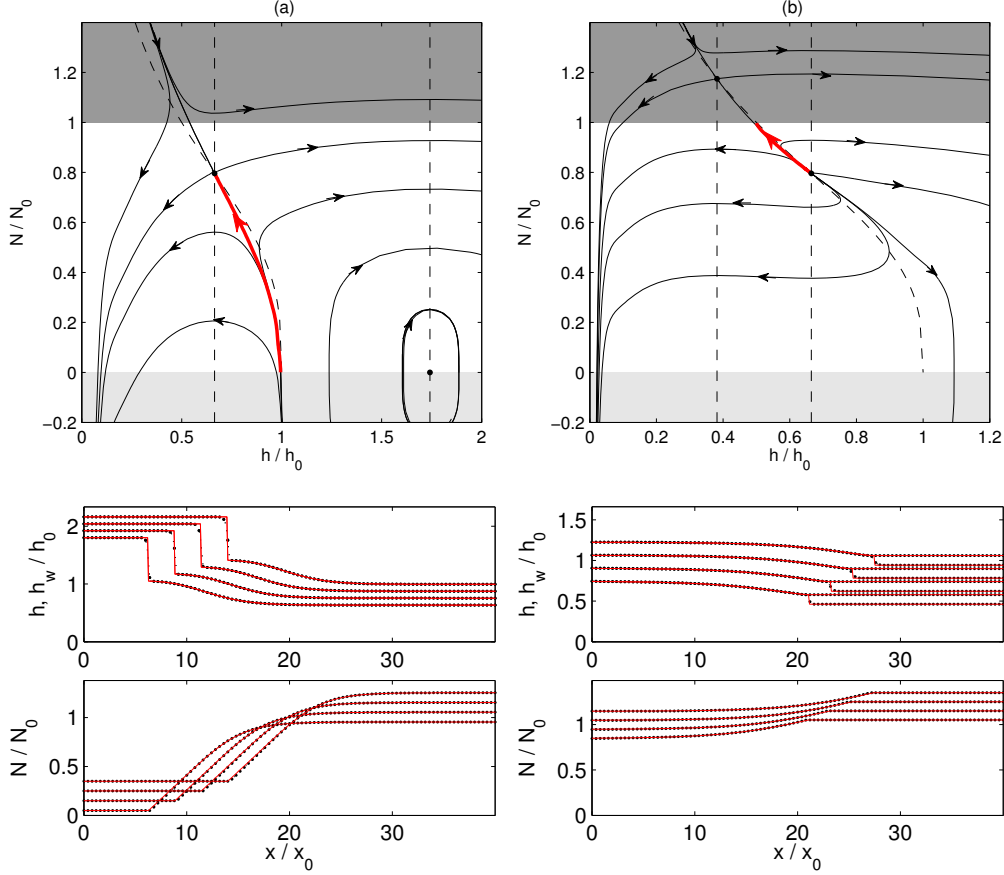
FIGURE 5. Travelling wave solutions with over- and underpressured regions. We have used the same scales as in figure 2, which now yields a three-parameter family of solutions, determined by the scaled fluxes q_+ and q_-, the length scale ratio ε, and the scaled overburden p_i. Here we set $\varepsilon = 1$ and $p_i/N_0 = 1$. In both columns, the top panel shows the phase plane with the same layout as in figure 2. The bottom two panels shows the actual travelling wave solutions $h(x, t)$ (as well as $h_w(x, t)$ where this differs from $h(x, t)$) and $N(x, t)$ at different times. For clarity, the solutions for h/h_0 are offset vertically at different times by amounts $0.06t/t_0$ and $0.08t/t_0$ in columns a and b, respectively, where $t_0 = \eta_0/V_0$. The solutions for N/N_0 are offset by $0.05t/t_0$ in both columns. Solutions are plotted for $t/t_0 = 1, 3, 5, 7$. Where there are two lines in the plots of h and h_w, the lower one represents h_w in an underpressured region. The solid lines in the bottom panels (red in the electronic version) correspond to the solution computed from phase plane analysis using an ordinary differential equation solver, while the dots show the solution computed numerically using the method in §4.3. The left-hand column (a) shows a solution with overpressure upstream ($q_- = 0.6q_0$ and $q_+ = 0.3q_0$), while the right-hand column (b) shows underpressure downstream ($q_- = 2q_0$ and $q_+ = 0.5q_0$).

downstream. An example of a solution of this type is shown in figure 5. We see that this solution, which is computed by means of an ordinary differential equation solver, is reproduced accurately by the mixed finite volume / finite element scheme of §4.3.

We can also compute travelling wave solutions in which a normally-pressured region upstream of $\eta = 0$ connects with an underpressured region downstream. In the under-
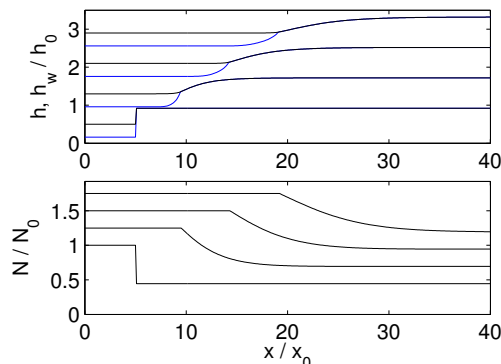
FIGURE 6. A region of underpressure upstream connected to a region of normal pressure downstream. The initial condition involves a jump in h and h_w at the junction between underpressure and normal pressure. Solutions are shown at times $t/t_0 = 0$, 5, 10, 15 with vertical offsets for N/N_0 of $0.05t/t_0$, and of $0.16t/t_0$ for h/h_0. The shock disappears and is replaced by an expansion fan in h_w on the underpressured side. Parameter values are $q_- = 0.1q_0$, $q_+ = 0.9q_0$, $\varepsilon = 1$, $p_i/N_0 = 1$.

pressured region, we have another constant solution

$$N = p_i, \qquad h = h_+ \text{ where } v_o(h_+) = v_c(h_+, p_i), \qquad h_w = h_{w+} < h_+ \qquad \text{for } \eta > 0. \tag{5.7}$$

In the normally-pressured region $\eta < 0$, we have $h_w = h$ and again the original travelling wave model (3.3) and (3.4) holds. (h, N) approaches the fixed $(h_-, N_-) = (h_{w-}, N_-)$ as $\eta \to -\infty$. It seems that we simply need to pick an orbit out of the fixed point, and trace this forward to the first point where $N = p_i$, this being the boundary $\eta = 0$ with the underpressured region. However, as in §3, the fixed point (h_{w-}, N_-) is an unstable spiral or centre for $h_{w-} > h_{w+}$. Therefore there appears to be an infinite choice of such orbits. However, at the boundary $\eta = 0$, we also need h to be continuous as h in this case satisfies (3.3) everywhere and, unlike h_w, cannot undergo abrupt jumps (such jumps are only permitted by (4.15)) if overpressure occurs, as in the above example). We therefore pick the unique orbit out of the fixed point that passes through the point $(h, N) = (h_+, p_i)$. A solution of this type is shown in figure 5. Once again, we have a shock at the boundary $\eta = 0$, and the solution is again reproduced accurately by the method described in §4.3.

Having seen that both travelling wave solutions contain shocks, it is worth noting that they both correspond to higher flux q_- entering from above than the flux q_+ leaving below. This constraint on fluxes also applies to the solutions in §3. The shocks we find are in fact similar to the free boundary in Hele-Shaw flows when there is expansion of the fluid-filled region (Howison 1992). The shocks have no analogue when more water flows out of the domain below than enters from above. This situation is similar to suction in negative squeeze films (e.g. Ockendon *et al.* 2003), and does not generate travelling wave solutions. Rather like the formation of 'mushy' regions in negative squeeze films, this situation tends to leave a partially fluid filled region Ω^e with no abrupt jump in fluid content at its boundary. An example of this is shown in figure 6.

5.2. *Steady states*

In one spatial dimension, it is also straightforward to find steady state solutions, which we can also use to test our numerical method and learn about the behaviour of the model. Take $m \geq 0$ to be prescribed, and assume that there is an upstream boundary at $x = 0$

with a prescribed inflow $q = q_n \geq 0$. To ensure that flow can always be in the positive x-direction including at overpressure, assume that $\mathrm{d}\phi_0/\,\mathrm{d}x < 0$. The steady-state version of (4.5) in one dimension demands that

$$\frac{\mathrm{d}q}{\mathrm{d}x} = m \tag{5.8}$$

and so

$$q(x) = -kh_w^\alpha \left| \frac{\mathrm{d}\phi}{\mathrm{d}x} \right|^{\beta-2} \frac{\mathrm{d}\phi}{\mathrm{d}x} = q_n + \int_0^x m(x')\,\mathrm{d}x' \tag{5.9}$$

is given. Finding steady states is a matter of integrating this equation.

For $\phi \leq \phi_0$, we can define a steady-state gap thickness $\mathcal{H}(\phi)$ from 2.4 implicitly through

$$v_o(\mathcal{H}(\phi)) = v_c(\phi_0 - \phi, \mathcal{H}(\phi)), \tag{5.10}$$

In addition, from 5.9 we can define water depth $\mathcal{H}_w(\,\mathrm{d}\phi/\,\mathrm{d}x)$ as a function of pressure gradient, as well as pressure gradient $\Psi(h_w)$ as a function of water depth through

$$\mathcal{H}_w(\Psi) = \left[\frac{q(x)}{k|\Psi|^{\beta-1}} \right]^{1/\alpha}, \tag{5.11}$$

$$\Psi(h_w) = - \left[\frac{q(x)}{kh_w^\alpha} \right]^{1/(\beta-1)}. \tag{5.12}$$

Using (5.9), the different cases in §4.1 can in steady state be summed up as

$$\frac{\mathrm{d}\phi}{\mathrm{d}x} = \begin{cases} \mathrm{d}\phi_m/\,\mathrm{d}x & \text{when } \phi = \phi_m \text{ and } \mathcal{H}_w(\,\mathrm{d}\phi_m/\,\mathrm{d}x) < \mathcal{H}(\phi_m) \\ \mathrm{d}\phi_0/\,\mathrm{d}x & \text{when } \phi = \phi_0 \text{ and } \mathcal{H}_w(\,\mathrm{d}\phi_0/\,\mathrm{d}x) > h_r \\ \Psi(\mathcal{H}(\phi)) & \text{when } \phi_m < \phi < \phi_0 \\ \min(\,\mathrm{d}\phi_m/\,\mathrm{d}x, \Psi(\mathcal{H}(\phi_m))) & \text{when } \phi = \phi_m \text{ and } \mathcal{H}_w(\,\mathrm{d}\phi_m/\,\mathrm{d}x) = \mathcal{H}(\phi_m) \\ \max(\,\mathrm{d}\phi_0/\,\mathrm{d}x, \Psi(h_r)) & \text{when } \phi = \phi_0 \text{ and } \mathcal{H}_w(\,\mathrm{d}\phi_0/\,\mathrm{d}x) \leq h_r \end{cases} \tag{5.13}$$

where the last two cases should be interpreted as giving the limiting value of the derivative taken as x is approached from below (or equally, the left-handed derivative at x). In the order given, the different cases correspond to the regions Ω^e, Ω^f, Ω_0^c, Ω_-^c and Ω_+^c, respectively. As a boundary condition, we impose a downstream glacier margin $x = x_m$ where water is at atmospheric pressure, $\phi(x_m) = \phi_m(x_m)$. All we need to do is integrate (5.13) backwards from there using an initial value problem solver.

A number of steady state solutions are shown in figures 7, 8 and 9. The computations shown use (2.5) as constitutive relations, with parameter values given in table 1. For each simulation, we show the potential ϕ computed from (5.13) as a function of position in the top panel (solid line), with the solution computed from the method in §4.3 as small dots. Clearly, in each case the solutions agree very closely, demonstrating that the numerical method chosen is successful for these settings. Also shown in each top panel are the region $\phi < \phi_m$ shaded in dark grey and the region $\phi > \phi_0$ in light grey. These are the under- and overpressure regions that ϕ in our model cannot enter. Note that ϕ_0 and ϕ_m are essentially proxies for bed elevation b and surface elevation s through (4.2) and (4.8). With a water density of $\rho_w = 1000$ kg m^{-3} and acceleration due to gravity of $g = 9.8$ m s^{-2}, a value of $\phi_m = 5$ MPa corresponds to a bed elevation of 510 m, while, with a density $\rho = 910$ kg m^{-3}, a difference between ϕ_0 and ϕ_m of 5 MPa corresponds to an ice thickness of 560 m; using this, it is straightforward to reconstruct the glacier geometry that corresponds to these figures (essentially, bed and surface are scaled versions of the boundaries of the grey regions in these plots). In the panel immediately below the

Parameter	$\tilde{A}$	n	h_r	l_r	u_b	k	α	β	ρ_w	ρ	g
value	5×10^{-25}	3	0.1	2	30	0.01	5/4	3/2	1000	910	9.8
units	$\mathrm{Pa^{-3}\,s^{-1}}$		m	m	$\mathrm{m\,a^{-1}}$	$\mathrm{m^{7/4}\,kg^{-1/2}}$			$\mathrm{kg\,m^{-3}}$	$\mathrm{kg\,m^{-3}}$	$\mathrm{m\,s^{-2}}$

TABLE 1. Parameter values for steady state calculations

plots of ϕ are the corresponding solutions for h and h_w (distinguishable when they are different by $h_w \leq h$). Solid lines indicate solutions derived from (5.13), dots are solutions computed from §4.3. The dashed horizontal line is $h = h_r$, which can only be reached at overpressure.

We have used three basic glacier shapes: a glacier with a 'plastic shape' (Nye 1951) given by

$$-\rho_i g(s - b)\frac{\partial s}{\partial x} = \tau_c \tag{5.14}$$

on an inclined planar bed $b(x) = b_0(1 - x/x_m)$ with $\tau_c = 10^5$ Pa, $b_0 = 1000$ m (figure 7) and a margin $s = b$ imposed at a finite position $x_m = 50$ km; a stepped bed (figure 8) and a bed that has almost zero thickness at the upstream end $x = 0$ as well as at the margin $x = x_m$ (figure 9). For each shape, we have computed steady states for different spatially uniform water input forcings m. The results are what one would expect: the larger m, the bigger the flux becomes, and the larger ϕ in the domain tends to be in order to open the ice-bed gap h and to generate a sufficiently large pressure gradient to evacuate the water being input. Naturally, this implies that overpressure is more common at larger water inputs, while smaller values of m, underpressure is more common.

The spatial pattern of over- and underpressure is also of interest. Flux increases towards the margin, and consequently so does the gap width h, making overpressure more common further downstream, especially for the 'plastic' shape of figure 7. However, ice thickness also tends to decrease towards the margin. In the absence of underpressure, the prescribed water input requires a certain gap width to flow out, which in turn corresponds to a certain effective pressure. Water pressures therefore need to decrease towards the margin to offset the decrease in ice overburden. As water pressures are bounded below, the partially-filled gap case is most common near the glacier margin. For the case of a glacier that also has vanishing thickness at its upstream end (figure 9), there is typically an underpressured region at $x = 0$ as well, especially for vanishing inflow $q_n = 0$.

The stepped glacier case (figure 8) is perhaps the most interesting as it has the most spatial structure. Where surface and bed drop steeply, we tend to find large potential gradients $-\mathrm{d}\phi/\mathrm{d}x$. For a given water input, this requires smaller water depth h_w than where the potential gradient is smaller, corresponding to higher effective pressures. Consequently, underpressure tends to occur first on these steep steps, especially at low water input. The converse is true of the flatter sections, where larger water depths h are needed. As water input is increased, overpressure tends to occur first on these flatter sections.

One notable feature of the steady state solutions is the occurrence of discontinuities in h_w at the downstream end of over- and underpressure regions. These are particularly obvious in panel d of figure 8 and panel b of figure 9, but can also be found elsewhere. These discontinuities are effectively stationary hydraulic jumps: flux across them is continuous, which is made possible by a discontinuity in hydraulic gradient that also occurs at the same location.
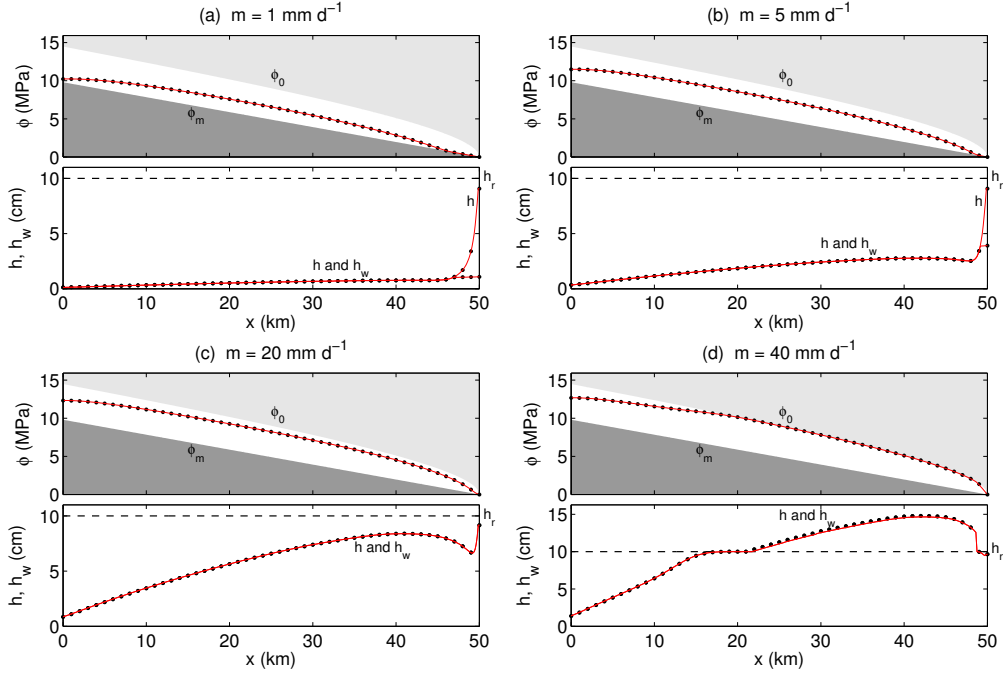
FIGURE 7. Steady state solutions for a plastic glacier. Each pair of panels corresponds to a different value of m as indicated in the bottom panel; $q_n = 0$ in each case. The top panel in each pair shows $\phi(x)$ computed from (5.13) as a solid line (red in the electronic version), with dots marking the numerical solution computed using the method in §4.3. The 'forbidden' regions $\phi < \phi_m$ and $\phi > \phi_0$ are shaded in heavy and light grey, respectively. Over- and underpressure occur where the solution $\phi(x)$ coincides with the boundaries of these regions. The bottom panel in each pair shows $h(x)$ and, if different, $h_w(x)$ below the curve for $h(x)$ (red in the electronic version), respectively. In other words, cavities are partially air-filled where the solid line splits in two, as is the case in the $m = 1$ mm d^{-1} case at 45 km. The horizontal dashed line in the bottom panels in each pair corresponds to the mean obstacle height h_r, so that complete bed separation occurs when solid line representing h rises above the dashed line, as is the case in the $m = 40$ mm d^{-1} case at 25 km. As before, solid lines show the solution computed from (5.13), and dots the solution obtained from §4.3, and we observe close agreement.

6. Discussion

We have presented a continuum model for distributed drainage under a glacier analogous to that Hewitt (2011) and similar to the model in Creyts & Schoof (2009). Under certain circumstances, this model as presented in §2 predicts unphysical results involving water pressure above overburden as well as negative water pressure. To remedy these, we have considered the physics that becomes relevant in these situations, leading to an extension of the original model that is able to capture ice-bed separation at zero effective pressure (which we have termed 'overpressure') as well as partial filling of cavities with air or water vapour at zero water pressure (or 'underpressure'). This extended model is a free boundary problem in which over- and underpressured regions are found as part of the solution. The centrepiece of this model is the determination of hydraulic potential (or equivalently, effective pressure) through the elliptic variational inequality (4.21). The closest analogue to our work in the glaciological literature is probably the model for partially filled channel flow in Schuler & Fischer (2009), though this is not explicitly formulated as a free boundary problem, and there is no analogue of the variational inequality (4.21) in their paper.
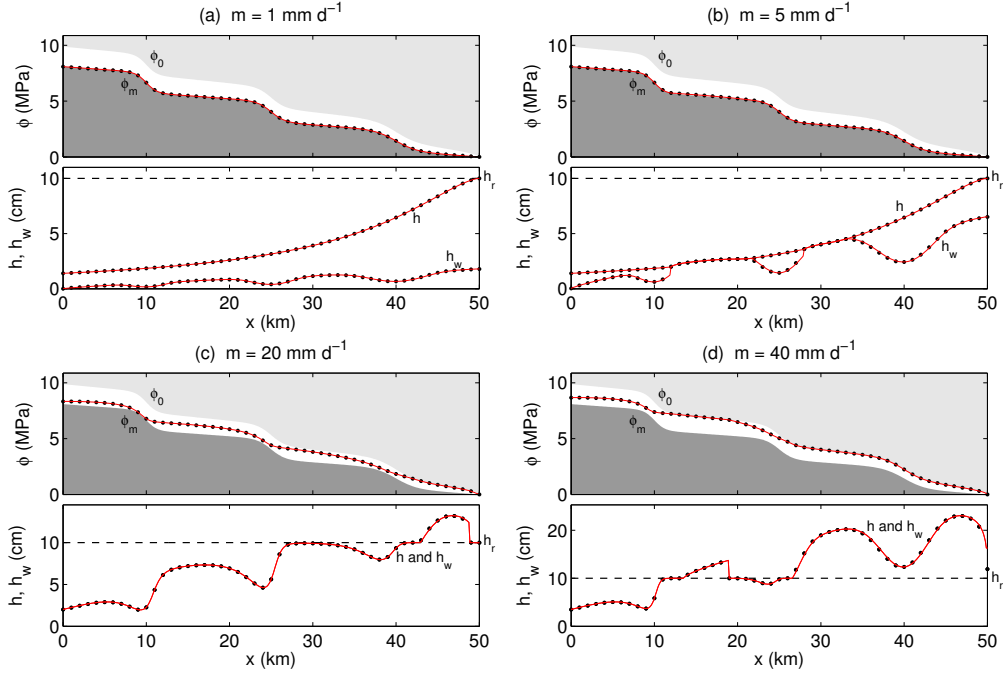
FIGURE 8. Steady state solutions for a stepped glacier, same line scheme as in figure 7. Again m is as indicated, with $q_n = 0$.
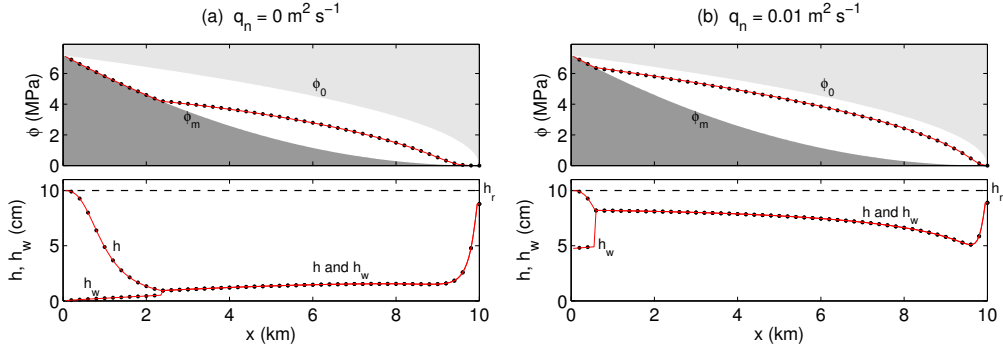

FIGURE 9. Steady state solutions for a glacier with zero thickness at the upstream end, same line scheme as in figure 7. Both cases have $m = 20$ mm d^{-1}, with inflow from upstream at $q_n = 0$ (a) and $q_n = 0.01$ m^2 s^{-1} (b).

To solve our model, we have devised the numerical method outlined in §4.3. This method is successful in reproducing the travelling wave and steady state solutions computed independently by means of ordinary differential equation initial value problem solvers in §5, but can undoubtedly be improved upon. Its most obvious drawback is the switch in solver for water depth h_w between different parts of the domain: on the over- and underpressured parts of the domain, a finite volume solver designed for hyperbolic problems is used, while an ordinary differential equation solver is employed in the normally-pressured regions in which the opening and closing relation (2.4) holds. If (2.4) and (4.5) were solved exactly, the two would give the same result, but in practice they correspond to fluxes that differ by an amount comparable to the discretization error.

To address this, we adjust the flux of $\mathbf{q}$ in (4.5) at boundaries between normally- and over- or underpressured finite volume cells so as to conserve mass. Our operator splitting approach naturally leads to a similar issue during recontact between water and ice, when the ice-bed gap in parts of the underpressured subdomain Ω^e fills up completely with water; our operator splitting scheme can lead to the computed water depth h_w exceeding the gap width h by a small amount when this happens, and again we adjust fluxes here to conserve mass, redistributing mass back into the partially filled region Ω^e. That said, some of our travelling wave and steady state solutions pertain to these case, and the numerical method used performs well for them. However, we have only tested the solution algorithm in one spatial dimension to date, though efforts to extend this to two dimensions are ongoing.

As may be expected, the model predicts that complete ice-bed separation and overpressure tends to occur at high fluxes and low surface and bed slopes, while underpressure is more common under thin ice, at low flux and in regions where surface and bed have steep downward slopes. This is the case for both the travelling wave and steady state solutions; our model gives us a way of confirming this expected result, and of computing the spatial extent and temporal evolution of over- and underpressure. A noticeable result of both the time-dependent travelling wave solutions as well as the steady state solutions, is the occurrence of shocks — abrupt changes in water depth — where overpressured flow turns into normally-pressured flow, and also where normally pressured flow turns underpressured (see §§5.1 and 5.2). Similar shocks were also found in the study of partially filled channel flow in Schuler & Fischer (2009).

There are recognizable similarities between our model and, for instance, free boundary problems in Hele-Shaw cells and in squeeze films (e.g. Ockendon *et al.* 2003). Aside from the turbulent closure scheme used in 4.4, which renders our elliptic problem (4.21) in p-Laplacian rather than Laplacian form (and therefore immediately removes the possibility of applying complex variable methods such as those in Howison (1992)), the main difference between our model and squeeze film models is that the gap width h not only changes over time (as is also the case in squeeze films but not in generic Hele-Shaw flows), but that the evolution of the gap width is related to pressure through (2.4), rather than being prescribed. However, similar phenomena occur in our model as in negative squeeze film models, such as the formation of 'mushy regions' — parts of the domain that are only partially filled with fluid. Although we have not attempted a complete mathematical analysis of our model, the ability to generate both travelling wave and steady state solutions gives us some confidence in its well-posedness.

While the main analogue of our underpressured regions lies in the mushy regions of negative squeeze films, our overpressured regions are more closely related to hydrofracturing (Tsai & Rice 2010). Our model is quite different from standard hydrofracture models, however. Based on the argument that regions of ice-bed separation are expected to be much larger than individual cavities, we assume that water pressure only has to exceed overburden by an insignificant amount to drive opening rates that are much larger than the opening rates of individual cavities, which provide the natural rate scale for our problem. Consequently, we assume regions of complete ice-bed separation to be 'afloat' in the sense that $p_w = p_i$ at normal rates of $\partial h/\partial t$. This may be inappropriate when water input is sufficiently rapid to require large opening rates, as may be the case when surface lakes flood to the base of a glacier or ice sheet. In this case, significant overpressure ($p_w > p_i$) may be required, with a gap opening rate controlled by bending moments in the overlying ice as is the case in hydrofracture models. The physics of our model would then suggest that the opening rate should be modelled as being due to viscous creep of the ice, while standard hydrofracture models consider the opening of gaps in

elastic media. At the short time scales at which we envisage a hydrofracture model being relevant, a viscoelastic description of ice may in fact be most relevant, with the elastic behaviour of Tsai & Rice (2010) applying in the limit of very short time scales. Further research will be necessary to delineate the situations where our model ceases to apply, and what alternatives can in that case best integrate hydrofracture into a large-scale subglacial drainage model.

A subtlety arises in the region Ω^c_+ of §4.1, where ice is still in contact with the bed, but overpressure $p_i = p_w$ has been reached. Here we assume that the same argument applies as in those regions Ω^f where complete ice-bed separation has been achieved, namely that the gap width h can increase essentially at arbitrary rates when p_w exceeds p_i by an infinitesimal amount. Implicit again is that the length scale limiting opening rates is the linear dimension of the region Ω^c_+, and is therefore large compared with the size of an individual cavity. As there is still partial contact between ice and bed in Ω^c_+, we are therefore assuming that ice and bed can easily separate when water pressure reaches overburden. The complication we have not considered is that a pressure gradient is generally required to drive water flow from the centre of cavities towards the cavity edges, where ice contacts the bed. Such a flow is necessary to widen the cavities and ultimately to lift ice off the bed. This pressure gradient is in fact one of the ingredients that controls crack tip migration in hydrofracture models, which would correspond to the migration of the cavity edges here. However, a pressure gradient of this type is actually needed not only in Ω^c_+, but also in the normally pressured regions, Ω^c_0 in §4.1, whenever cavities are expanding. Implicit in our continuum model was the ability to define a pressure variable $p_w(x, y, t)$ on the macroscopic scale, therefore implying that p_w is approximately constant at the cavity scale; in other words, we have assumed that the intra-cavity pressure differences required to allow cavities to expand (and, presumably, shrink) are small, and we simply assume that this holds in the incipient overpressure region Ω^c_+ too. To test this will ultimately require a sophisticated model for dynamic cavities that takes into account the flow of water within cavities necessary to allow the change of shape (while the cavity models of Schoof (2005) and Gagliardini *et al.* (2007) are essentially steady-state models that make no reference to water pressure gradients within the cavities).

Physically, we expect underpressured drainage systems to occur close to glacier margins, under steep sections of glacier, such as ice falls, or where water discharge is low. Thin ice will allow substantial cavities to exist even at zero water pressure, so that the hydraulic gradient generated by bed slope alone may be enough to evacuate a given discharge without filling the cavities. This is obviously more likely when bed slopes, or discharge is small. Our results in §5.2 are consistent with this intuition. By contrast, one would expect overpressurization to result mostly from relatively abrupt increases in water supply to a drainage system whose permeability is at least initially too small to accommodate the additional water supply. This is likely to happen during so-called 'spring events', when seasonal melt water first reaches the bed at the end of winter Iken & Bindschadler (1986), or during some flooding events derived from sub- or supraglacial lakes (Björnsson 2002; Flowers *et al.* 2004; Das *et al.* 2008).

In practice, overpressurization is not likely to persist because the drainage system will adapt, either through the opening over time of cavities (which our model can describe) or through the formation of channels (which it cannot as posed in this paper). The latter will happen if there is insufficient bed roughness h_r to allow large enough cavities to form, which in the absence of channelization then requires persistently overpressured regions. The latter situation, with cavity size being too limited, is evident in some of our simulations in figures 7 and 8: the steady state solutions computed there require

overpressured regions to persist indefinitely. This would however correspond to water flowing as a contiguous film. In reality, heat will be dissipated in the flow, and the dissipation of heat should naturally drive a channelizing instability. This occurs through a feedback between increased water film thickness, increased heat dissipation, and melting of the overlying ice leading to further thickening of the film (Walder 1982). A similar runaway can also occur at finite effective pressure, when water flows through individual cavities rather than a contiguous film (e.g. Walder 1986; Kamb 1987; Schoof 2010, see also appendix A), although the closing rate v_c is now non-zero and increases with cavity size, which also allows cavities to exist stably (Creyts & Schoof 2009; Schoof 2010; Hewitt 2011). In the companion paper (Hewitt *et al.*, 2011, submitted), we tackle channelization both at overpressure and normal pressure by coupling the model for distributed drainage developed here with a discrete formulation for channels of the type used in Schoof (2010) and Hewitt (2011).

Appendix A. Linked cavities with channel-like orifices

The model for linked-cavity drainage developed in Fowler (1987) posits that, while cavity size may be controlled through a balance between opening and closing as encapsulated by (2.1), and hence by (2.4) in a continuum formulation, the connections between cavities that control flow are not. The flux prescription (2.10) therefore differs from what Fowler's model would predict. In that model, these connections (labelled 'orifices') are controlled by a balance between dissipation-driven melting and viscous closure. Denoting orifice cross-section by S_R, we have an evolution equation of the form

$$\frac{\mathrm{d}S_R}{\mathrm{d}t} = \frac{k_R}{\rho_i L} S_R^\alpha |\Psi|^{3/2} - A S_R f(N)^n, \tag{A 1}$$

where k_R is a friction factor, L is the latent heat of melting for ice, Ψ is the hydraulic gradient along the orifice, and $f(N)$ is the *local* effective pressure at the orifice, which Fowler takes to differ potentially from N due to enhanced normal stresses in the contact areas between larger cavities. A particular feature of his model is, while one might be tempted to put $f(N) = N$, Fowler argues that $f(N)$ may actually be a decreasing function of N under some circumstances. The discharge Q_R through the orifice is then

$$Q_R = k_R S_R^\alpha |\Psi|^{\beta-2}\Psi \tag{A 2}$$

An obvious continuum formulation of the above is then to define an orifice size density $h_R = S_R/l_r$, where l_r is still the spacing between cavities. The evolution of h_R is controlled not by (2.4) but by

$$\frac{\partial h_R}{\partial t} = \frac{k}{\rho_i L} h_R^\alpha |\nabla\phi|^\beta - A h_R f(N)^n \tag{A 3}$$

where $k = k_R l_r^{\alpha-1}$ and to replace (2.10) by

$$\mathbf{q} = k h_R^\alpha |\nabla\phi|^{\beta-2}\nabla\phi. \tag{A 4}$$

However, it is easy to show that the amended model consisting of (2.4), (2.8) along with (A 3) and (A 4) is unconditionally unstable to runaway melt enlargement of the orifices described by h_R, with no wavelength selection in the instability (and in particular, no suppression of short wavelengths). The physical interpretation is that the model is prone to channelization of conduits flowing in parallel as explored in Schoof (2010, see supplementary material), and is not in fact a viable continuum model. This is the case regardless of whether $f(N)$ increases or decreases with N.

To see this, consider a flow down an inclined plane with background hydraulic gradient Ψ_0 as in §3, but admit the possibility of variations in h, h_R and N in the lateral direction y. Suppose there is a mean discharge q_0 in the x-direction through the system. The steady state solution is then spatially uniform. Steady state orifice size $\bar{h}_R$ satisfies

$$\bar{h}_R \equiv \left(\frac{q_0}{k\Psi_0^{\beta-1}} \right)^{1/\alpha}, \tag{A 5}$$

with steady state effective pressure $\bar{N}$ and cavity water storage $\bar{h}$ given implicitly by

$$Af(\bar{N})^n = \frac{k}{\rho_i L}h_R^{\alpha-1}|\Psi_0|^{3/2}, \qquad v_0(\bar{h}) = v_c(\bar{h}, \bar{N}). \tag{A 6}$$

For simplicity, we can consider only the special case of perturbations depending on y but not x (i.e., the limit of long wavelengths in the x-direction), putting

$$h_R = \bar{h_R} + h_R' \exp(\sigma t + i\kappa y), \quad h = \bar{h} + h' \exp(\sigma t + i\kappa y), \qquad N = \bar{N} + N' \exp(\sigma t + i\kappa y).$$

Linearizing, we get

$$\sigma h_R' = \left[\alpha \frac{k}{\rho_i L}h_R^{\alpha-1}|\Psi_0|^\beta - Af(\bar{N})^n \right] h_R' - Anf(\bar{N})^{n-1}f'(\bar{N})N' \tag{A 7a}$$

$$\sigma h' = \left[v_{o,h}(\bar{h}) - v_{c,h}(\bar{h}, \bar{N}) \right] h' - v_{c,N}(\bar{h}, \bar{N})N' \tag{A 7b}$$

$$\sigma h' = -\frac{(\beta-1)q_0}{\Psi_0}\kappa^2 N' \tag{A 7c}$$

This has one mode in which $h' = N' = 0$, for which the growth rate is

$$\sigma = \alpha \frac{k}{\rho_i L}h_R^{\alpha-1}|\Psi_0|^\beta - Af(\bar{N})^n.$$

For $\alpha > 1$, it is clear from (A 6) that $\sigma > 0$, and that the growth rate is further independent of wavenumber κ. In effect, this is the same result as in the instability for discrete, parallel channels as in section 2.1 of the supplementary material in Schoof (2010); importantly, the conclusion that orifices are unstable is independent of the sign of $f'(\bar{N})$. The above indicates that Fowler's linked cavity model ought to be unstable to channelization, and not amenable to a continuum treatment of the form we envisage above. Instead, a discrete treatment of flow paths as described in Schoof (2010) as well as in the companion paper (Hewitt *et al.*, 2011, submitted) becomes necessary. The essential difference between Fowler's picture of the drainage system and ours is that we assume that flow-limiting constrictions between larger cavities are still controlled by the same opening and closing processes as those larger cavities themselves, whereas Fowler appeals to the mechanics of subglacial channels.

REFERENCES

ALLEY, R.B. & BINDSCHADLER, R.A., ed. 2001 *The West Antarctic Ice Sheet: Behaviour and Environment*, Washington, D.C. American Geophysical Union.

BARTHOLOMEW, I., NIENOW, P., MAIR, D., HUBBARD, A., KING, M.A. & SOLE, A. 2010 Seasonal evolution of subglacial drainage and acceleration in a Greenland outlet glacier. *Nature Geoscience* **3**, 408–411.

BJÖRNSSON, H. 2002 Subglacial lakes and jökulhlaups in Iceland. *Global and Planetary Change* **35**, 255–271.

BUDD, W.F., KEAGE, P.L. & BLUNDY, N.A. 1979 Empirical studies of ice sliding. *J. Glaciol.* **23** (89), 157–170.

CLARKE, G.K.C. 1976 Thermal regulation of glacier surging. *J. Glaciol.* **16** (74), 231–250.

CLARKE, G.K.C. 1996 Lumped-element analysis of subglacial hydraulic circuits. *J. Geophys. Res.* **101** (B8), 17547–17559.

CREYTS, T.T. & SCHOOF, C.G. 2009 Drainage through subglacial water sheets. *J. Geophys. Res.* **114** (F04008), doi:10.1029/2008JF001215.

CUFFEY, K.M., CONWAY, H., HALLET, B., GADES, T.M. & RAYMOND, C.F. 1999 Interfacial water in polar glaciers and glacier sliding at -17° c. *Geophys. Res. Lett.* **26** (6), 751–754.

DAS, S.B., JOUGHIN, I., BEHN, M.D., HOWAT, I.M., KING, M.A., LIZARRALDE, D. & BHATIA, M.P. 2008 Fracture propagation to the base of the Greenland ice sheet during supraglacial lake drainage. *Science* **320**, 778–781.

EKELAND, I. & TEMAM, R. 1976 *Convex Analysis and Variational Problems*. Amsterdam: North-Holland.

ENGELHARDT, H. & KAMB, B. 1997 Basal hydraulic system of a West Antarctic ice stream: constraints from borehole observations. *J. Glaciol.* **43** (144), 207–230.

EVANS, L.C. 1998 *Partial Differential Equations*. Providence: American Mathematical Society.

FLOWERS, G.E. 2008 Subglacial modulation of the hydrograph from glacierized basins. *Hydrological Processes* **22**, 3903–3918.

FLOWERS, G.E., BJÖRNSSON, H., PALSSON, F. & CLARKE, G.K.C. 2004 A coupled sheet-conduit mechanism for jökulhlaup propagation. *Geophys. Res. Lett.* **31** (5), L05401.

FLOWERS, G.E. & CLARKE, G.K.C. 2002 A multi-component model of glacier hydrology. *J. Geophys. Res* **107** (2287), doi:10.1029/2001JB001122.

FLOWERS, G.E., MARSHALL, S.J., BJÖRNSSON, H. & CLARKE, G.K.C. 2005 Sensitivity of Vatnajökull ice cap hydrology and dynamics to climate warming over the next 2 centuries. *J. Geophys. Res.* **110** (F2), F02011.

FOWLER, A.C. 1986 A sliding law for glaciers of constant viscosity in the presence of subglacial cavitation. *Proc. R. Soc. Lond. A* **407**, 147–170.

FOWLER, A.C. 1987 Sliding with cavity formation. *J. Glaciol.* **33** (105), 255–267.

FOWLER, A.C. 1989 A mathematical analysis of glacier surges. *SIAM J. Appl. Math.* **49** (1), 246–263.

FOWLER, A.C. 2009 Instability modelling of drumlin formation incorporating lee-side cavity growth. *Proc. R. Soc. Lond. A* **465** (2109), 2681–2702.

FOWLER, A.C., MURRAY, T. & NG, F.S.L. 2001 Thermally controlled glacier surging. *J. Glaciol.* **47** (159), 527–538.

GAGLIARDINI, O., COHEN, D., RABACK, P. & ZWINGER, T. 2007 Finite-element modeling of subglacial cavities and related friction law. *J. Geophys. Res.* **112** (F2), F02027, doi:10.1029/2006JF000576.

GLOWINSKI, R. 1984 *Numerical Methods for Nonlinear Variational Problems*. New York: Springer-Verlag.

HEWITT, I.J. 2011 Modelling distributed and channelized subglacial drainage: the spacing of channels. *J. Glaciol.* **57** (202), 302–314.

HEWITT, I.J. & FOWLER, A.C. 2008 Seasonal waves on glaciers. *Hydrological Processes* **22**, 3919–3930.

HOWAT, I.M., TULACZYK, S., WADDINGTON, E. & BJÖRNSSON, H. 2008 Dynamic controls on glacier basal motion inferred from surface ice motion. *J. Geophys. Res.* **113** (F03015), doi:10.1029/2007JF000925.

HOWISON, S.D. 1992 Complex variable methods in Hele-Shaw moving boundary problems. *Euro. J. Appl. Math* **3**, 209–224.

HUBBARD, B., SHARP, M.J., WILLIS, I.C., NIELSEN, M.K. & SMART, C.C. 1995 Borehole

water-level variations and the structure of the subglacial hydrological system of Haut Glacier d'Arolla, Valais, Switzerland. *J. Glaciol.* **41** (139), 572–583.

IKEN, A. & BINDSCHADLER, R.A. 1986 Combined measurements of subglacial water pressure and surface velocity of Findelengletscher, Switzerland: conclusions about drainage system and sliding mechanism. *J. Glaciol.* **32** (110), 101–119.

IVERSON, N.R., BAKER, R.W., HOOKE, R.LEB., HANSON, B. & JANSSON, P. 1999 Coupling between a glacier and a soft bed: I. A relation between effective pressure and local shear stress determined from till elasticity. *J. Glaciol.* **45** (149), 31–40.

JANSSON, P. 1995 Water pressure and basal sliding on Storglaciären, northern Sweden. *J. Glaciol.* **41** (138), 232–240.

KAMB, B. 1987 Glacier surge mechanism based on linked cavity configuration of the basal water conduit system. *J. Geophys. Res.* **92** (B9), 9083–9100.

KAMB, B., RAYMOND, C.F., HARRISON, W.D., ENGELHARDT, H., ECHELMEYER, K.A., HUMPHREY, N., BRUGMAN, M.M. & PFEFFER, T. 1985 Glacier surge mechanism: 1982–1983 surge of Variegated Glacier, Alaska. *Science* **227** (4686), 469–479.

KIKUCHI, N. & ODEN, J.T. 1988 *Contact problems in elasticity : a study of variational inequalities and finite element methods*. Philadelphia: SIAM.

KINDERLEHRER, D. & STAMPACCHIA, G. 1980 *An Introduction to Variational Inequalities and their Applications*. New York: Academic Press.

LAPPEGARD, G., KOHLER, J., JACKSON, M. & HAGEN, J.O. 2006 Characteristics of subglacial drainage system deduced from load-cell measurements. *J Glaciol.* **52** (176), 137–147.

LLIBOUTRY, L. 1968 General theory of subglacial cavitation and sliding of temperate glaciers. *J. Glaciol.* **7** (49), 21–58.

MACAYEAL, D.R. 1993 Binge/purge oscillations of the Laurentide Ice Sheet as a cause of North Atlantic Heinrich events. *Paleoceanography* **8** (6), 775–784.

NYE, J.F. 1951 The flow of glaciers and ice-sheets as a problem in plasticity. *Proc. R. Soc. Lond. A* **207** (1091), 554–572.

NYE, J.F. 1976 Water flow in glaciers: jökulhlaups, tunnels and veins. *J. Glaciol.* **17** (76), 181–207.

OCKENDON, J.R., HOWISON, S.D. & LACEY, A.A. 2003 Mushy regions in negative squeeze films. *Quart. J. Mech. Appl. Math.* **56** (3), 361–379.

PATERSON, W.S.B. 1994 *The Physics of Glaciers*, 3rd edn. Oxford: Pergamon.

PIMENTEL, S. & FLOWERS, G.E. 2010 A numerical study of hydrologically driven glacier dynamics and subglacial flooding. *Proc. R. Soc. Lond. A* **467** (2126), 537–558.

RÖTHLISBERGER, H. 1972 Water pressure in intra- and subglacial channels. *J. Glaciol.* **11** (62), 177–203.

SCHOOF, C. 2005 The effect of cavitation on glacier sliding. *Proc. R. Soc. Lond. A* **461**, 609–627, doi:10.1098/rspa.2004.1350.

SCHOOF, C. 2007*a* Cavitation on deformable glacier beds. *SIAM J. Appl. Math.* **67** (6), 1633–1653.

SCHOOF, C. 2007*b* Pressure-dependent viscosity and interfacial instability in coupled ice-sediment flow. *J. Fluid Mech.* **570**, 227–252.

SCHOOF, C. 2010 Ice-sheet acceleration driven by melt supply variability. *Nature* **468**, 803–806.

SCHULER, T.V. & FISCHER, U.H. 2009 Modeling the dirunal variation of tracer transit velocity through a subglacial channel. *J. Geophys. Res.* **114**, F04017, doi:10.1029/2008JF001238.

SHEPHERD, A., HUBBARD, A., NIENOW, P., KING, M., MACMILLAN, M. & JOUGHIN, I. 2009 Greenland ice sheet motion coupled with daily melting in late summer. *Geophys. Res. Lett.* **36** (L01501), doi:10.1029/2008GL035785.

TSAI, V.C. & RICE, J.R. 2010 A model for turbulent hydraulic fracture and application to crack propagation at glacier beds. *J. Geophys. Res.* **115** (F03007), doi:10.1029/2009JF001474.

VAN DE WAL, R.S.W., BOOT, W., VAN DEN BROEKE, M.R., SMEETS, C.J.P.P., REIJMER, C.H., DONKER, J.J.A. & OERLEMANS, J. 2008 Large and Rapid Melt-Induced Velocity Changes in the Ablation Zone of the Greenland Ice Sheet. *Science* **321**, 111–113.

WALDER, J.S. 1982 Stability of sheet flow of water beneath temperate glaciers and implications for glacier surging. *J. Glaciol.* **28** (99), 273–293.

WALDER, J. 1986 Hydraulics of subglacial cavities. *J. Glaciol.* **32** (112), 439–445.